
Modeling the Dust Distribution in the Proto-Planetary Disk IM Lup

Anirudh Sharma



München 2020

Modellierung der Staubverteilung in der protoplanetaren Scheibe IM Lup

Anirudh Sharma

Master Thesis
an der Fakultät für Physik
der Ludwig-Maximilians-Universität
München

vorgelegt von
Anirudh Sharma
aus Delhi Cantt, India

München, den 11. März 2020

Supervisor: Prof. Tilman Birnstiel

Contents

Abstract	vii
1 Introduction	1
1.1 Motivation	1
1.2 IM Lup	1
1.3 Recent Observations	2
1.3.1 DSHARP	2
1.3.2 DARTTS-S	2
1.3.3 Inclination and Position angle	3
1.4 Geometry of the Disk	3
2 Radiative Transfer	5
2.1 Flux, Intensity and the Planck Function	5
2.2 The Formal Transfer Equation	6
2.3 Scattering	8
3 RADMC-3D and Opacities	11
3.1 RADMC-3D - The Radiative Transfer Code	11
3.2 Opacities	12
3.2.1 Mean Opacities	13
4 Disk Structure and Setup	15
4.1 1D Disk	15
4.2 2D disk	17
4.3 Dust	19
5 Comparison of Different Vertical and Temperature Setups	21
5.1 Vertical Density Profile	21
5.2 Temperature Profile	21
5.3 Radial Intensity	24
5.4 Setup Time	25

6 Images and Radial Intensity Profiles	27
6.1 Synthetic Images	27
6.2 Radial Profiles	27
6.2.1 Disk Mass	29
6.2.2 Grain Sizes	29
7 Monte Carlo Markov Chains and Parameter Estimation	33
7.1 The χ^2 value	33
7.2 MCMC Algorithm	34
7.3 Without scattered light	35
7.4 With scattered light	39
8 Conclusion	47
Acknowledgments	51

Abstract

Understanding the dust distribution and how it effects observations is essential in understanding planet formation. With this motivation, this work tries to model the dust distribution in the protoplanetary disk IM Lup. IM Lup has been observed in both the mm and the near-infrared (scattered light) wavelengths and shows a vastly different geometry in the two observations with respect to both radial and vertical extents.

Before modelling IM Lup directly, some experiments related to the disk setup have been carried out. The vertical structure along with the temperature calculation was setup using three different techniques with differing levels of complexity. It was found that the effect on the temperature, vertical density and radial intensity profiles is marginal despite vastly different setup times.

Additionally, results confirm that increasing disk mass leads to a proportional increase in the mm intensity but has negligible effect on the scattered light intensity of the disk. Also, larger dust grains proportionally increase the mm intensity whereas the smaller dust grains are responsible for the scattered light intensity.

The disk has been parametrised and to obtain the optimum values of the parameters and the associated uncertainty, the Monte-Carlo Markov-Chain algorithm has been used. The algorithm was successful in optimising the parameters of the disk when only the mm continuum is considered but failed to optimise when both the mm and the scattered light observations were considered for fitting. The samples obtained do not fit well the observations and have a high uncertainty associated with them. The possible reasons and solutions have been discussed.

Chapter 1

Introduction

1.1 Motivation

In the past decade, the launch of the Kepler space telescope has confirmed the ubiquitous nature of exoplanets. But the question of how these planets form from the dust in protoplanetary disk is still a long way from being answered. The key to answering this question is to first understand the dust distribution (both in space and particle size) in the disk which will help further answer the question of how the dust interacts with itself to form planetesimals.

This work attempts to answer the first part by modelling the dust distribution in the proto-planetary disk IM Lup. The objective is to constrain the dust properties, density and size as a function of the disk radius.

1.2 IM Lup

IM Lup is a Class II protoplanetary disk found in the Lup II star forming region. Some general facts are given in table 1.1

Position (J2000) [16]	15 56 09.17658 -37 56 06.1193
Distance (pc)	158 ± 3
$\log T_{\text{eff}}$ (K)	3.63 ± 0.03
$\log L (L_{\odot})$	0.41 ± 0.20
$\log t_{*}$ (years)	5.7 ± 0.4
$\log \dot{M}_{*} (M_{\odot} \text{ year}^{-1})$	-7.9 ± 0.4

Table 1.1: Basic properties of the IM Lup. All values apart from the position are from [1]

1.3 Recent Observations

In the past couple of years, highly resolved images of the disk have been taken as part of the DSHARP [2] and DARTTS-S [3] survey.

1.3.1 DSHARP

The Disk Substructures at High Angular Resolution Project (DSHARP) conducted with the Atacama Large Millimeter/submillimeter Array (ALMA), found and characterized substructures for 20 nearby protoplanetary disks using observations at the 1.25mm (240 GHz) continuum emission. The resolution for the observation is ~ 35 mas.

Shown here is the image of IM Lup in the continuum emission as well the deprojected and azimuthally averaged radial intensity profile as obtained from DSHARP.

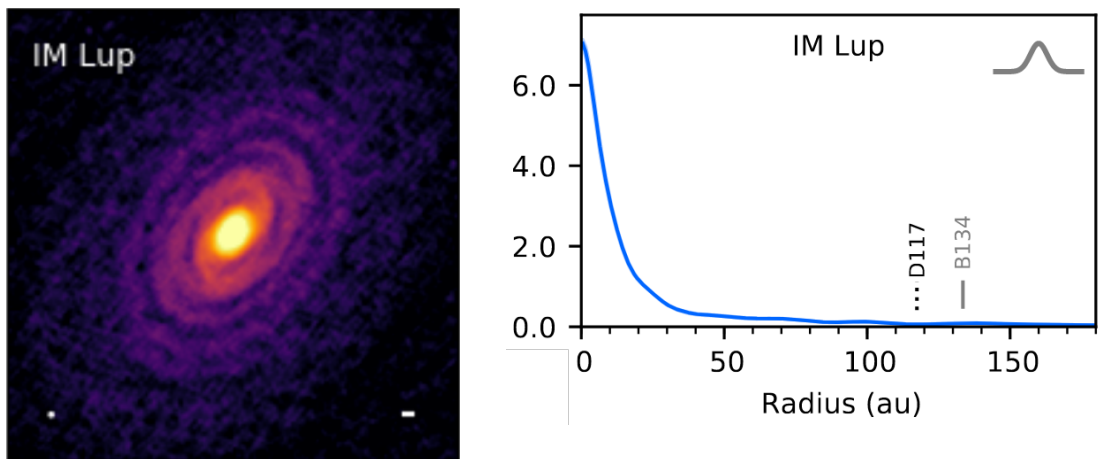


Figure 1.1: The 1.25mm continuum image from DSHARP survey (left) and the radial intensity profile in mJy beam^{-1} (right). D117 and B134 are the dark and bright bands respectively identified by DSHARP

In the 1.25mm regime the disk is expected to be mostly optically thin (except close to the star). As a result the disk in the image appears to be flat due to most of the emission coming from dust being present in the midplane.

1.3.2 DARTTS-S

The Disks ARound TTauri Stars with SPHERE (DARTTS-S) survey are observations of eight TTauri stars with strong mm and sub-mm excesses using SPHERE/IRDIS telescope in the J ($1.25\mu\text{m}$) and H ($1.65\mu\text{m}$) bands. In these wavelengths the disk is expected to be optically thick and the observed light is dominated by light scattered by the dust grains further away from the disk. As a result this gives essential insights into the vertical and

3-D structure of the disk.

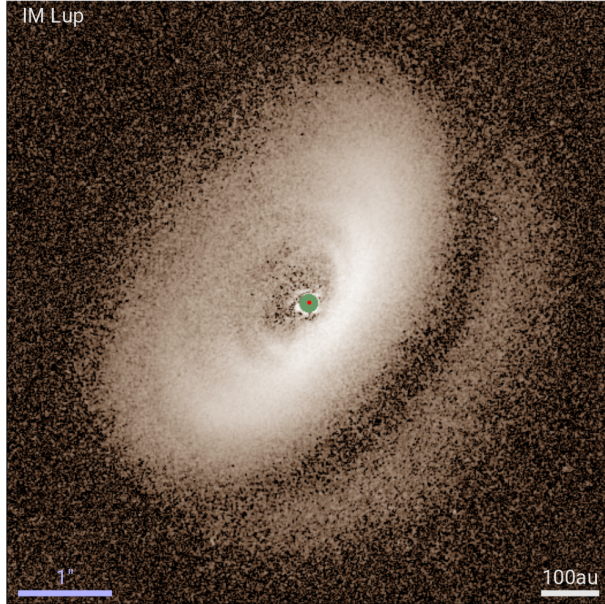


Figure 1.2: H-band image for IM Lup as obtained from DARTTS-S

1.3.3 Inclination and Position angle

These surveys also calculated some geometrical features of the disk. The position angle found by the two surveys seem to be consistent with each other with DSHARP suggesting the average position angle for the two substructures to be $144.55^\circ \pm 0.65^\circ$. The inclination estimate for the surveys seems to be inconsistent with DSHARP suggesting $47.5^\circ \pm 0.5^\circ$ and DARTTS-S suggesting $56^\circ \pm 2^\circ$. In this study the inclination from DSHARP has been used since it has been found using a flat disk instead of a flared disk and has less uncertainty associated with it.

1.4 Geometry of the Disk

The images in the two wavelengths show an incredible difference in the geometry of the two disks. In the near-infrared the disk shows strong flaring and an obvious vertical structure. This suggests that there are dust grains in the upper parts of the disk which are prevented from settling down by turbulence. The size of these dust grains is expected to be small since they are well coupled with the gas and are optically thin in the mm image. The mm image on the other hand shows a flat disk which suggests that the larger dust grains are well settled to the mid-plane.

The radial extent of the disk is also something which differs in the two images. The mm image suggests that the disk is 290au large whereas the near-infrared image extending to as wide as 400au which suggests that there is a radial separation of the different sized dust in addition to the vertical separation.

These two extreme geometries in the two wavelengths should be useful in constraining the distribution of the dust.

Chapter 2

Radiative Transfer

Before the disk is physically setup, one needs to understand how light interacts with a protoplanetary disk. Radiative transfer is the description of how light travels through media and the energy transfers which take place in the form of absorption, emission and scattering. Since light is the only information one receives from far off objects, understanding the behaviour of light becomes crucial in Astronomy. Through this behaviour one can interpret the properties of the medium. In this study as well, the properties of the dust (quantity, size distribution, space distribution) have been concluded based on how light from the central star interacts with this dust in the proto-planetary disk.

This chapter goes into some of the details of radiative transfer.

2.1 Flux, Intensity and the Planck Function

Flux or radiative flux is defined as the energy (in this context in the form of electromagnetic radiation) passing through a unit area per unit time. It is represented by the symbol F and its CGS units are $\text{erg s}^{-1} \text{ cm}^{-2}$.

But when dealing with light we are often interested in how much energy is carried by a small wavelength window since our images are usually taken with a narrow wavelength filter. In such a case the flux from wavelength between λ and $\lambda + \Delta\lambda$ divided by $\Delta\lambda$ is considered. This quantity is called **spectral flux density** or monochromatic flux or simply flux (in which case the previous quantity is called bolometric flux instead of flux). The symbol to represent is F_λ and the units are $\text{erg s}^{-1} \text{ cm}^{-3}$. The relation between the monochromatic flux and the bolometric flux is given by

$$F = \int_0^\infty F_\lambda d\lambda \quad (2.1)$$

Often, the monochromatic flux is expressed as the flux per small frequency range instead of wavelength range. In such a case the bolometric flux is the integral of F_ν over the entire frequency range and the CGS unit is $\text{erg s}^{-1} \text{ cm}^{-2} \text{ Hz}^{-1}$.

$$F = \int_0^{\infty} F_{\nu} d\nu \quad (2.2)$$

An old astronomical unit to express monochromatic flux is the Jansky (Jy). The conversion of a Jansky to CGS units is given by

$$1 \text{ Jy} = 10^{-23} \text{ erg s}^{-1} \text{ cm}^{-2} \text{ Hz}^{-1} \quad (2.3)$$

The flux is an extremely useful physical quantity when looking at point objects in the sky. But in the case of extended objects, it doesn't manage to convey all the information. For example, if an object A covers twice as much area as object B in the sky but both have the same flux, object A would appear to be dimmer. In order to account for this dimness the flux is divided by unit solid angle of the source object. The resulting quantity is called **radiant intensity** or intensity with symbol I and unit $\text{erg s}^{-1} \text{ cm}^{-2} \text{ sr}^{-1}$. Now for the previously discussed objects A and B, A would have an intensity half of that of B.

Similar to flux, intensity can also be expressed in a monochromatic form. This quantity is called the monochromatic intensity or spectral intensity or just like the flux case, simply intensity (in which case the radiant intensity is called bolometric intensity). The symbols is either I_{λ} or I_{ν} depending on whether one is working with wavelengths or frequencies. The units are $[\text{erg s}^{-1} \text{ cm}^{-3} \text{ sr}^{-1}]$ or $[\text{erg s}^{-1} \text{ cm}^{-2} \text{ Hz}^{-1} \text{ sr}^{-1}]$ respectively. They could also be expressed using the definition of Jansky as Jy/sr.

A body which is at thermal equilibrium with temperature T and absorbs all the light falling on it emits an intensity which is function of the temperature. This intensity is known as the **blackbody radiation** and it is given by the **Planck function**

$$I_{\nu} = B_{\nu}(T) = \frac{2h\nu^3/c^2}{e^{h\nu/kT} - 1} \quad (2.4)$$

The bolometric flux of a blackbody is given by the Stefan-Boltzmann law

$$F = \sigma_{SB} T^4 \quad (2.5)$$

where $\sigma_{SB} = 5.67 \times 10^{-5} \text{ erg s}^{-1} \text{ cm}^{-2} \text{ K}^{-4}$.

2.2 The Formal Transfer Equation

The principle interest is to understand and quantify how a ray of light made of photons interacts with the medium through which it passes. The interaction takes place in the form of absorption, emission and scattering. Each of these would be addressed one at a time.

Suppose a cloud through which light is passed. This cloud is only absorbing in nature. As a photon passes through the average path length it travels before being absorbed is

called the mean free path l . The mean free path is a function of frequency and is therefore represented by l_ν and its dimension and unit are same as that for length. The denser the cloud, more likely and quicker is a photon going to be absorbed. As a result a denser cloud would have a shorter l_ν . In a bulk sense, the mean free path indicates the decrease in intensity for a ray of light. A ray of light passing through a cloud which has a thickness of nl_ν would have its intensity reduced by e^{-n} . This decrease in intensity is called extinction. The number of mean free paths the ray has to travel is called the **optical depth** (τ) of the cloud. When $\tau \ll 1$ then the cloud is said to be optically thin and when $\tau \gg 1$ the cloud is optically thick.

Another way to represent the mean free path is through its reciprocal $1/l_\nu = \alpha_\nu$, which is called the **extinction coefficient** or **opacity**. When a cloud is not homogeneous then the opacity would be a function of the space $\alpha_\nu(s)$ and the optical depth across two points in space can be found using

$$\tau_\nu = \int_{s_0}^{s_1} \alpha_\nu(s) ds \quad (2.6)$$

Since the opacity is proportional to the density of the cloud, it can also be expressed as $\alpha_\nu = \rho k_\nu$. When dealing with proto-planetary disks, we usually work with surface densities instead of densities. In such a case the opacity is taken proportional to the surface density $\alpha_\nu = \Sigma k_\nu$. Note that the symbol for both proportionality constants is k_ν . This constant is called the mass-weighted opacity or simply opacity (which adds further to the confusion).

The decrease in intensity when a ray passes through a small distance is the opacity $\alpha_\nu(s)$ times the intensity.

$$\frac{dI_\nu(s)}{ds} = -\alpha_\nu(s) I_\nu(s) \quad (2.7)$$

This is the **formal transfer equation** in the case the cloud is only absorbing. On integrating this equation the intensity as a function of the location in the cloud can be expressed as

$$I_\nu(s_1) = I_\nu(s_0) e^{-\tau_\nu} \quad (2.8)$$

But a cloud is never only absorbing. It would add some radiation of its own to the light ray as well. In such a case, an emission term is added to the formal transfer equation.

$$\frac{dI_\nu(s)}{ds} = j_\nu(s) - \alpha_\nu(s) I_\nu(s) \quad (2.9)$$

where j_ν is called the **emissivity** and has the units [$\text{erg s}^{-1} \text{cm}^{-3} \text{Hz}^{-1} \text{sr}^{-1}$]. It is convenient to express j_ν as $S_\nu \alpha_\nu$ where S_ν is called the source function. The formal transfer equation then becomes

$$\frac{dI_\nu(s)}{ds} = \alpha_\nu(s) [S_\nu(s) - I_\nu(s)] \quad (2.10)$$

In case the cloud is at a local thermodynamic equilibrium i.e. the temperature in the cloud is not time varying the source function is the blackbody radiation.

$$\frac{dI_\nu(s)}{ds} = \alpha_\nu(s)[B_\nu(T(s)) - I_\nu(s)] \quad (2.11)$$

This equation demonstrates that the intensity of a ray in a cloud under LTE would try to approach the blackbody radiation at the given temperature.

2.3 Scattering

Scattering is the absorption of photons by the irregularities on a surface or a medium and then immediately being re-emitted again. The re-emitted light could be in different directions and of different intensities.

The principle way in which scattering differs from a simple absorption and emmission event is that the cross section of absorption (probability of light ray being absorbed) is angle dependent and the emitted light tends to be polarised. This can be understood by looking at the incoming light as an electromagnetic wave and the incident material to be dielectric. The presence of the electromagnetic wave polarises the material i.e. the charges inside the material align to make many dipoles. And these dipoles in turn make their own electromagnetic wave which is proportional to the incoming electromagnetic wave. The materials response to the incoming wave is quantified by the **complex index of refraction**.

$$m(\lambda) = n(\lambda) + ik(\lambda) \quad (2.12)$$

The term n is the absorption contribution and k is the scattering contribution to the total refractive index. The values of these refractive indices can be found out experimentally for different materials.

In order to formalise the polarisation and angular dependence of scattering, a vector description of light propagation is required. A beam of radiation and its polarisation can be fully described by its **Stokes parameters**

$$I = E_{x',0}^2 + E_{y',0}^2 \quad (2.13)$$

$$Q = E_{x',0}^2 - E_{y',0}^2 \quad (2.14)$$

$$U = 2E_{x',0}E_{y',0} \cos \Delta \quad (2.15)$$

$$V = 2E_{x',0}E_{y',0} \sin \Delta \quad (2.16)$$

Here $E_{x',0}$ and $E_{y',0}$ are the amplitude of the electric field plane wave in the x and y axis which are the two axes perpendicular to the direction of propagation n . Δ is the phase difference between the x and y plane waves. The parameter I describes the total intensity of the beam of light and Q , U and V describe the polarisation state. If $Q = U = V = 0$

then the light is unpolarised. The Stoke parameters are often represented as a column vector called the Stokes vector

$$\begin{pmatrix} I \\ Q \\ U \\ V \end{pmatrix}.$$

Using the vector notation, for given incoming light (I, Q, U, V) and the subsequent light after scattering (I', Q', U', V') can be equated to each other using a scattering matrix.

$$\begin{pmatrix} I' \\ Q' \\ U' \\ V' \end{pmatrix} = \begin{pmatrix} Z_{11} & Z_{12} & Z_{13} & Z_{14} \\ Z_{21} & Z_{22} & Z_{23} & Z_{24} \\ Z_{31} & Z_{32} & Z_{33} & Z_{34} \\ Z_{41} & Z_{42} & Z_{43} & Z_{44} \end{pmatrix} \begin{pmatrix} I \\ Q \\ U \\ V \end{pmatrix} \quad (2.17)$$

This scattering matrix which operates on a Stokes vector is called a **Muller Matrix**.

For spherical particles and/or a large number of randomly oriented particles and applying **Mie Theory**, the scattering matrix simplifies to the following form with only four terms

$$\begin{pmatrix} Z_{11} & Z_{12} & 0 & 0 \\ Z_{12} & Z_{11} & 0 & 0 \\ 0 & 0 & Z_{33} & Z_{34} \\ 0 & 0 & -Z_{34} & Z_{33} \end{pmatrix} \quad (2.18)$$

which can be calculated using experimental observations.

Note:- Mie theory is a theory which explains the scattering behaviour of a spherical particle in the regime where the wavelength of light is similar to or larger to the particle size.

Chapter 3

RADMC-3D and Opacities

3.1 RADMC-3D - The Radiative Transfer Code

The radiative transfer code used in this work is RADMC-3D [8]. The task of a radiative transfer code is to create images of an astrophysical set-up and to calculate the temperature structure. In this study, a protoplanetary disk with a dust distribution of different sized grains has been set-up. RADMC-3D has been used to simulate the images of the models and the simulated images are then compared to the observed images (see chapter 1).

The typical input for RADMC-3D includes, a spacial grid, density of different dust species as a function of space, the associated opacities of these dust species, properties of the star and a range of wavelengths for which the calculations need to carried out.

The first step of the radiative transfer procedure is to calculate the temperature of the dust species given the spacial configuration and the heating source. (Note:- This step can be skipped if one would like to calculate temperature in a different manner). This is done by simulating the emission a very large number of photons from the source star in a random direction in the space grid. As it moves through the grid it interacts with the dust particles and could get either absorbed (in which case a photon would be re-emitted based on the temperature) or scattered. How these interactions take place is determined by the opacities and densities of the dust species. The photon packet keeps on bouncing around in the grid until it crosses the edges of the grid. Every time the photon packet interacts with the dust its temperature increases. In turn, hotter dust would emit more radiation. If enough photon packets are simulated through the grid, this temperature of every dust species would reach an equilibrium (same amount of energy coming in versus going out) and this is the output of this routine.

Simulating images happens in a similar way, but with a couple key differences. Firstly, an image is usually made at a fixed wavelength and as a result the photon packages which are emitted would be of this wavelength specifically. Secondly, the vantage point of the

observer needs to be mentioned with respect to the inclination and the position angle of the object. Similar to the temperature calculation procedure, emitted photons trace their path through the grid and then the image is calculated based on the photon packets being emitted towards the observer.

3.2 Opacities

Opacities play a key role in the light-dust interaction. At the same time it is extremely hard to precisely know the composition and structure of the dust in a proto-planetary disk. For this work, the opacities from DSHARP [4] have been used. The opacities are easily available as an open-source software and include a full-scattering Mie formulation of the opacities as well. For the opacity calculation, dust is assumed to be a mixture with the following constituents:-

Material	Density [g/cm ³]	Mass fraction	Volume Fraction	Source
Water ice	0.92	0.2000	0.3642	[17]
Astronomical Silicates	3.30	0.3291	0.1670	[7]
Troilites	4.83	0.0743	0.0258	[12]
Refractory organics	1.5	0.3966	0.4430	[12]

The combined density of the mixture is 1.675 g/cm³. Calculating the combined opacity of the mixture is not straight forward and depends on the structure of the composition of the dust particles. This calculation is included in the software. The resultant opacities as a function of wavelength are shown below.

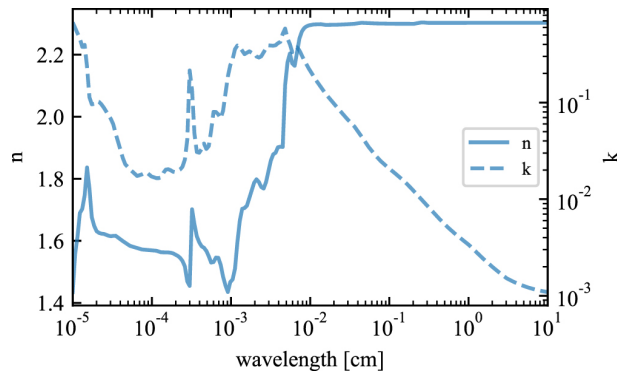


Figure 3.1: Effective optical constants of the dust [4] with n being the absorption contribution and k being the scattering contribution to the opacity. Together they contribute to the refractive index

The opacities are a function of not only the wavelength but also the size of the dust particles. In the proto-planetary disk, one expects to find a continuous range of dust sizes

between a minimum (a_{min}) and a maximum (a_{max}) dust grain size. The exact distributions across different sizes is an interplay between the coagulation and the fragmentation and is hard to calculate analytically. It is nonetheless typically assumed to be a power-law.

$$n(a) \propto a^{-q} \text{ where } a_{min} < a < a_{max} \quad (3.1)$$

The value of q is usually taken as 3.5 [14] or 2.5 [6]. Since different sizes have different opacities, the amount of dust in each size plays a key role in how the disk interacts with the star light. One of the objectives of this work is the constrain the value of q for disk IM Lup. This has been discussed in the subsequent chapters.

3.2.1 Mean Opacities

One way to deal with opacities is to look at mean opacities i.e. opacities which have been averaged over all wavelengths. There are two ways to formulate the mean opacities which are the Planck mean opacity and the Rosseland mean opacity

$$\bar{\kappa}_{Planck}(T) = \frac{\int_0^{\infty} \kappa_{\nu} B_{\nu}(T) d\nu}{\int_0^{\infty} B_{\nu}(T) d\nu} \quad (3.2)$$

$$\bar{\kappa}_{Rosseland}(T) = \left(\frac{\int_0^{\infty} \frac{1}{\kappa_{\nu}} \frac{dB_{\nu}(T)}{dt} d\nu}{\int_0^{\infty} \frac{dB_{\nu}(T)}{dt} d\nu} \right)^{-1} \quad (3.3)$$

The mean opacity takes away the direct relation between the opacity and the wavelength. But at the same time it becomes a function of the temperature. As a result with a change in temperature the mean opacity would change all else being kept same. These formulations can be useful when a quick and dirty (and not completely incorrect) radiative transfer solution is needed since independent transfers do not need to take place for each wavelength.

Chapter 4

Disk Structure and Setup

This chapter deals with the description of the physical set-up of the disk before it is fed into RADMC-3D. This was done with the help of the python library DISKLAB (not yet published) which has been developed by Cornelis Dullemond and Til Birnstiel. It is a library of routines and methods which would be typically used in the setting up of a protoplanetary disk.

4.1 1D Disk

1D disk contains all information about the disk as a function of radius. These include quantities like gas and dust surface densities (Σ_g and Σ_d respectively), the flaring angle (which contains information of about the disk vertical structure) and so on. The properties of the central star are the same as those mentioned in table 1.1. The inner edge of the disk is at a radius of 0.1au and the value of the viscosity parameter alpha is taken as 10^{-3} .

The radial surface density is set by the simplified Lynden-Bell Pringle (LBP) profile as mentioned in [15]

$$\Sigma = \Sigma_c \left(\frac{r}{R_c} \right)^\gamma \exp \left[- \left(\frac{r}{R_c} \right)^{2-\gamma} \right] \quad (4.1)$$

where Σ_c is a normalization for the total disk mass, γ is the exponent of the LBP model, R_c is the critical radius beyond which the density drops off exponentially. The values of the parameters and how they impact the disk observation have been discussed later.

The total dust surface density of the dust is typically taken to be 1% of the gas density. The contribution of the different sized dust to the total dust surface density is given by previously discussed equation 3.1.

The vertical extent of a protoplanetary disk is expressed by the pressure scale height

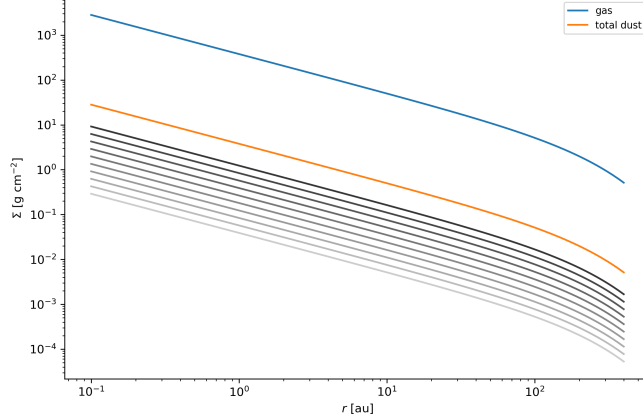


Figure 4.1: The radial density of the gas and dust in the disk which extends till 400au. The critical radius is 300au, Σ_c is 2.6gm/cm² and γ is 0.87. The grey lines are the surface densities of 10 dust species in the disk with the darker lines corresponding to larger dust sizes.

of a disk which is the ratio of the sound speed to the Keplerian angular speed.

$$H_p = \frac{c_s}{\Omega} = \left(\frac{kTr^3}{\mu m_H GM_*} \right)^{1/2} \quad (4.2)$$

The height of a disk is not discrete and tapers as one goes further away from the mid-plane. The above expression comes from balancing the vertical pressure of the gas with the gravitation force towards the mid plane. The gas density profile from this derivation is

$$\rho(z) = \frac{\Sigma}{\sqrt{2\pi}H} \exp\left(-\frac{1}{2}\left(\frac{z}{H}\right)^2\right) \quad (4.3)$$

In a 1D disk since the vertical information is contained in the form of H_p and the temperature as T_{mid} which is a function of radius.

The two terms H_p and T_{mid} are coupled with each other. The height of the disk as a function of radius would directly impact the amount of starlight that it can intercept. The amount of starlight it can intercept would increase the temperature which would result in the disk height increasing. As a result the height and the temperature need to be self-consistent with each other and are calculated iteratively.

Another measure for the height of a disk is the surface height (H_s) which is defined as the height at which the optical depth of the disk becomes 1. Using this H_s the flaring index (ξ) is defined as

$$\xi(r) = \frac{d\ln(H_s/r)}{d\ln r} \quad (4.4)$$

And this is related to the flaring angle ($\phi(r)$) [5])

$$\phi(r) = \frac{0.4R_*}{r} + \xi(r) \frac{H_s}{r} \quad (4.5)$$

For a 1D disk setup, a constant flaring angle of 0.05 is used as an initial input and then solved for iteratively along with the mid-plane temperature and other height related parameters. There are ways to set the disk height more robustly and these are discussed in the subsequent section.

4.2 2D disk

The 1D disk can be converted into a 2D disk by adding information in a vertical direction at every radial grid point. Again the most important properties which relate to the temperature and the dust and gas densities. These can now be calculated and stored in a 2D way.

The vertical gas density follows hydrostatic equilibrium (eq. 4.3). The gas temperature is a required input and its calculation to varying levels of approximation are now discussed here. Given a certain starting density structure, the stellar radiation would hit the disk at an angle which is the flaring angle, from where it would penetrate towards the midplane. The optical depth of the disk to this stellar radiation is given by

$$\tau(z) = \int_z^\infty \frac{\rho_d(z') \kappa_{P,*}}{\phi} dz' \quad (4.6)$$

where ρ_d is the dust density and κ_P is the planck mean opacity at stellar wavelengths. The flux of stellar radiation at a height z in the disk at a distance r from the star is

$$F_*(z) = \frac{L_*}{4\pi r^2} e^{-\tau(z)} \quad (4.7)$$

The mean intensity at a height z is

$$J_*(z) = \frac{F_*(z)}{4\pi} \quad (4.8)$$

It is assumed that the albedo of the dust is zero and all the flux absorbed is re-emitted. The source function for the re-emission is

$$q(z) = \phi \frac{dF_*(z)}{dz} \quad (4.9)$$

This radiation would diffuse out in all directions and the mean intensity of this diffusion J_{diff} can be calculating the first moment H_{diff}

$$\frac{dH_{diff}(z)}{dz} = \frac{q(z)}{4\pi} \quad (4.10)$$

$$\frac{dJ_{diff}(z)}{dz} = -3\rho_d\kappa_R H_{diff}(z) \quad (4.11)$$

where κ_R is the Rosseland mean opacity. Finally, the temperature (assumed to be same for the gas and all dust species) as a function of the height z can be calculated as

$$T(z) = \left(\frac{\pi}{\sigma_{SB}} (J_{diff}(z) + \frac{\kappa_{P,*}}{\kappa_P(T)} J_*(z)) \right)^{1/4} \quad (4.12)$$

where σ_{SB} is the Stephan-Boltzmann constant and $\kappa_P(T)$ is the Planck mean opacity of the dust at Temperature T .

This method is called the **1+1D** approach since the only source of radiation for a vertical slice is from the top surface and the radiation moving from one vertical slice to the next is ignored.

An even more robust way is to not have the stellar radiation from the top surface but also from the neighbouring vertical slice. In order to formalise this approach, the introduction of a dimensionless vertical coordinate ζ is required. ζ is the aspect ratio (z/r) and is defined so because stellar radiations move across the disk with a constant aspect ratio. The flux of the stellar radiation at every point in the disk can then be calculated by

$$F_*(r, \zeta) = \frac{L_*}{4\pi(r^2 + z^2)} e^{-\tau(r, \zeta)} \quad (4.13)$$

And the optical depth $\tau(z, \zeta)$ is given by

$$\tau(r, \zeta) = \sqrt{1 + (\zeta)^2} \int_{R_*}^r \rho_d(r', \zeta) \kappa_{P,*} dr' \quad (4.14)$$

The calculated flux (and therefore intensity) can be plugged into eq 4.12 to calculate the temperature. This approach is termed as the **2D-1** approach.

For the formulation to be even more complete, the re-emission (eq 4.11) from the dust grains should also be treated in a 2D way.

$$\vec{H} = -\vec{\nabla} J \frac{f}{3\rho_d\kappa_R} \quad (4.15)$$

where f is a value from the flux-limited diffusion theory from [13]. This is the **2D-2** approach.

The vertical structure and the temperature determination can be done by any of these methods. The performance of these has been discussed in chapter 5.

Given that setting up the self-consistent vertical structure is an iterative process, there are actually no guarantees that the process would converge for a given disk with certain

parameters. Instabilities are always possible. For example a case where a certain part of the disk has a higher vertical extent than what's beyond it. In such a case (depending on the routine used) it could happen that the disk immediately beyond this high part stops receiving any heat and as a result just collapses to a very small height and low temperatures. Damping the amount of change (in density or temperature) across every iteration could be a way to get rid of the instability and make the disk converge.

4.3 Dust

So far, during the set-up of the vertical structure, special emphasis has not been given to the dust. It has just assumed to be 1% of the gas density. But this is not true when it comes to the vertical structure. Dust is constantly stirred around by turbulent processes in the disk. The stirring eventually reaches a steady state such that the rate of settling matches the rate of the dust rising due to the turbulence. The vertical profile of the dust can be calculated by solving the following equation from [10]

$$\frac{\partial}{\partial z} \left(\ln \frac{\rho_d}{\rho_g} \right) = - \frac{\Omega^2 \tau_s z}{D} \quad (4.16)$$

Ω is the Keplerian angular velocity, τ_s is the stopping time of a dust particle facing head wind and is given by

$$\tau_s = \frac{\text{Dust particle mass density} \times \text{Particle size}}{\text{Gas density} \times \text{Sound speed}} \quad (4.17)$$

D is the diffusion coefficient and is taken as

$$D = \frac{\alpha c_s H_p}{S_c} \quad (4.18)$$

where S_c is the Schmidt number which has been measure to be around 1. Larger dust is expected to settle closer to the mid-plane whereas smaller dust is expected to be further away. Therefore the presence of these smaller dust grains is essential for the flaring geometry which is seen in the scattered light image.

The distribution across the different sizes is taken to be a power law.

$$n(a) \propto a^{-q} \text{ where } a_{min} < a < a_{max} \quad (4.19)$$

The normalisation of this power gets fixed by the gas density and the dust to gas ratio.

The value of a_{max} as a function of radius is also parametrised by a power law.

$$a_{max}(r) = A \left(\frac{r}{\text{AU}} \right)^{-B} \quad (4.20)$$

This is because due to higher radial drift of larger dust particles, a disk is expected to be depleted of larger particles the further one moves away from the star (See plots)

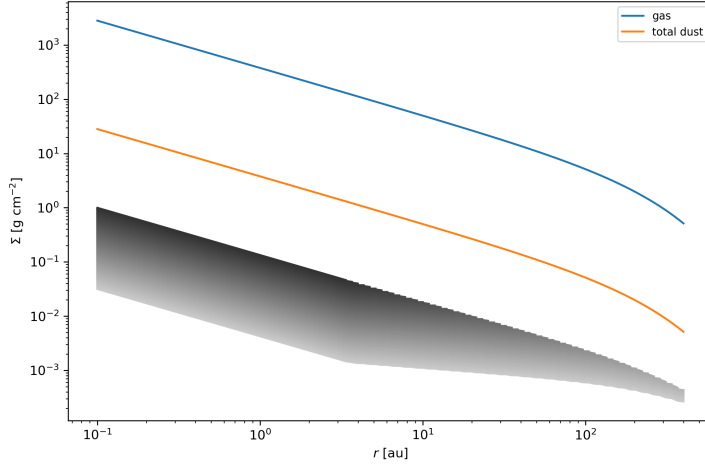


Figure 4.2: The radial density of a disk with parameters similar to fig 4.1 but containing a hundred dust species logarithmically spaced between 10^{-5} and 10^{-1} cm with the darker shade representing a larger particle size. As one moves away from the star the darker shades start to disappear and the smaller sized particles start having a larger proportion of the total dust density. The total dust density remains 1% of the gas density

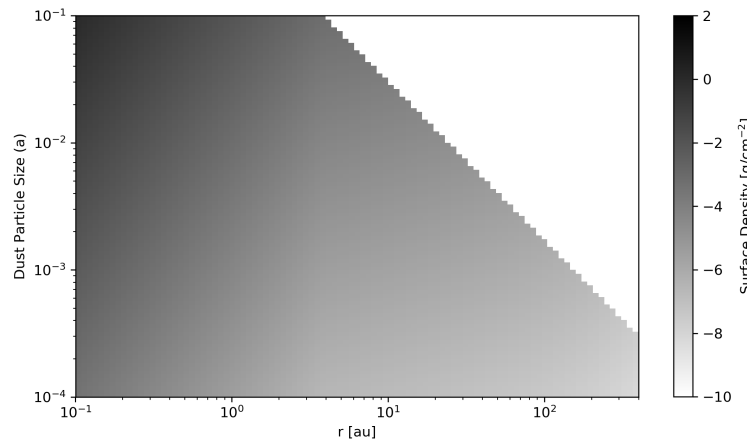


Figure 4.3: The plot shows the same information as the previous plot. But this time the colours represent the density, with darker colours representing a higher density. The larger particles, which are higher on the y axis, stop being present in the disk after a certain a radius with the cut-off radius being smaller for larger dust grains

The values of the parameters q , A , B is something which would be explored and discussed further on.

Chapter 5

Comparison of Different Vertical and Temperature Setups

In the previous chapter, different techniques for setting the vertical structure and the temperature of the disk were discussed. This chapter will discuss how these different setups perform with respect to time and accuracy.

For comparison, the parameters for the disk need to be fixed. The Σ_c and γ from the LBP profile are taken as 2 and 0.75 respectively. 20 dust sizes have been considered ranging from 10^{-5} to 10^{-1} cm equally spaced in the log scale. The amount of dust across different sizes determined by parameter q (eq 3.1) has a value 3.5. Dust to gas ratio is fixed at 1% throughout the disk. a_{max} is taken constant across the radius of the disk.

5.1 Vertical Density Profile

Shown in fig 5.1 are the plots for the density profile of the dust across the disk for the three methods.

The three density profiles look very similar to each other with the the 1D+1 and 2D-1 being nearly identical. The 2D-2 disk does seem to be slightly puffed up within a radius of 100 au.

5.2 Temperature Profile

The plots of the vertical profiles for the three methods are shown in fig 5.2. The different temperature profiles are very similar to each other. Especially close to the disk edge (where disk turns from optically thick to thin).

To understand the temperature and density more closely, the vertical profiles have been plotted in fig 5.3 at a radius of 51.89au. The dust density for all the three methods is very

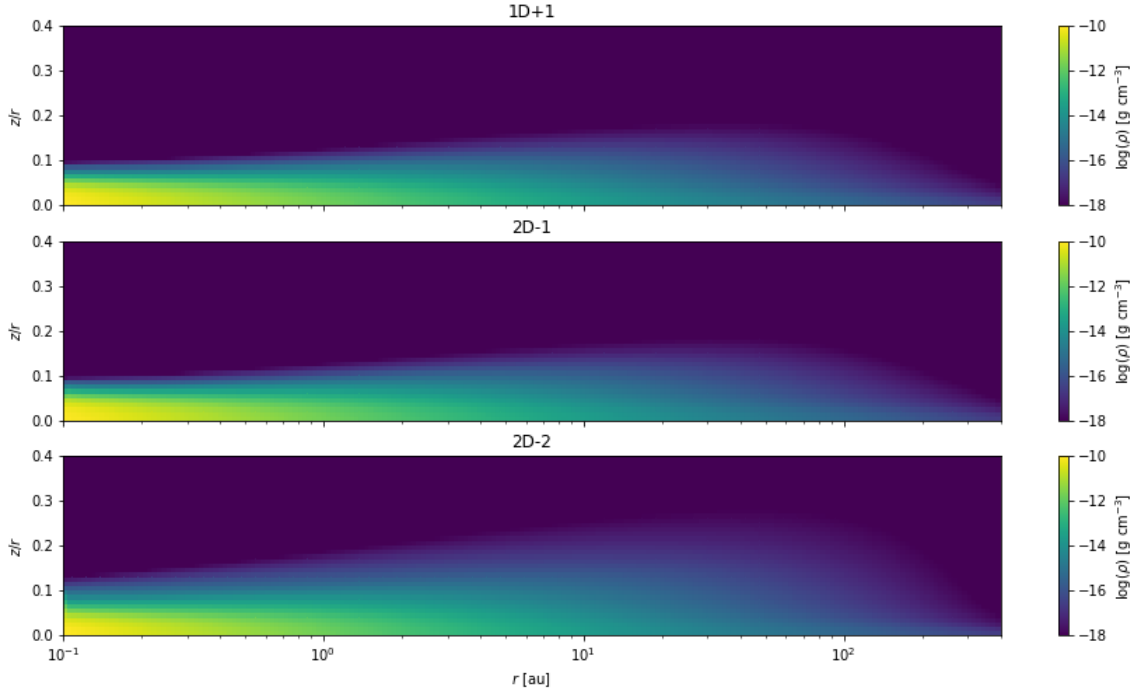


Figure 5.1: The density profiles of the dust obtained by different vertical settling methods

similar and drops to close to 0 within a height of 10au. At this distance is also where the disk becomes optically thin and the temperature increases. The temperature within 10au is about 3K higher for the 2D-2 method compared to the other two.

Till now, only radiative diffusion methods have been discussed to find the temperature of the disk. One can also use a full radiative transfer code, from RADMC-3D, to find out the temperature (termed MC therm). In such a case the individual opacities of the different sized dust grains are taken independently instead of a mean opacity. The temperature of all the dust sizes are as a result decoupled and not the same. It is expected to work well in optically thin regions where enough photon packets enter and exit for the grid cell to reach an equilibrium temperature but in optically thicker regions like the disk mid-plane the temperature calculation is expected to be noisy. The comparison of the mid-plane temperatures is shown in fig 5.4. The three diffusion temperatures are consistent with each other. The MC therm temperature has been plotted for the mid-sized dust grain. It shows a higher temperature at the outer parts of the disk.

The full radiative transfer in this work has only been used to calculate the final temperature of the dust species and not to actually set up the vertical density and temperature profiles because it takes much longer to carry out. The time taken by each method are discussed subsequently in section 5.4.

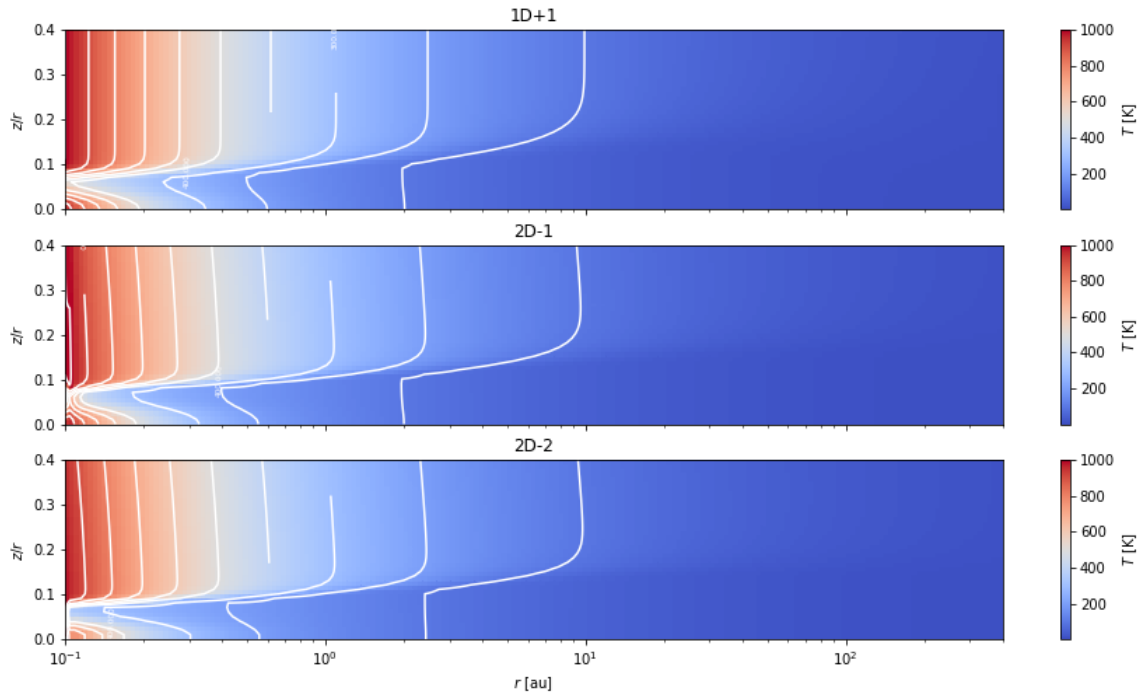


Figure 5.2: The temperature profiles within the disk by different vertical settling methods

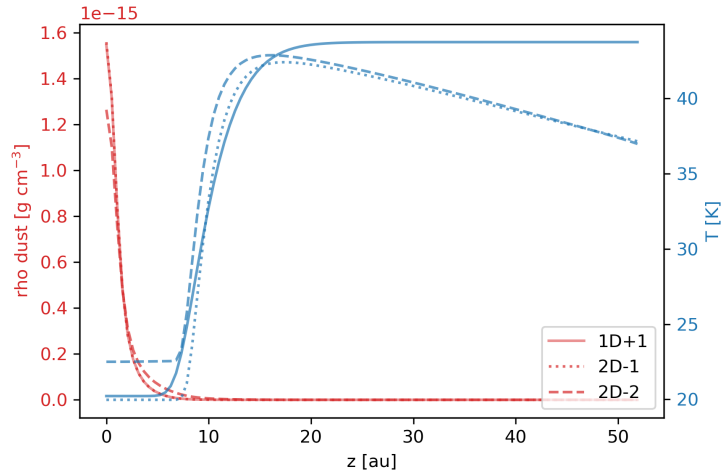


Figure 5.3: The vertical density and the temperature at a distance of 51.89au from the star

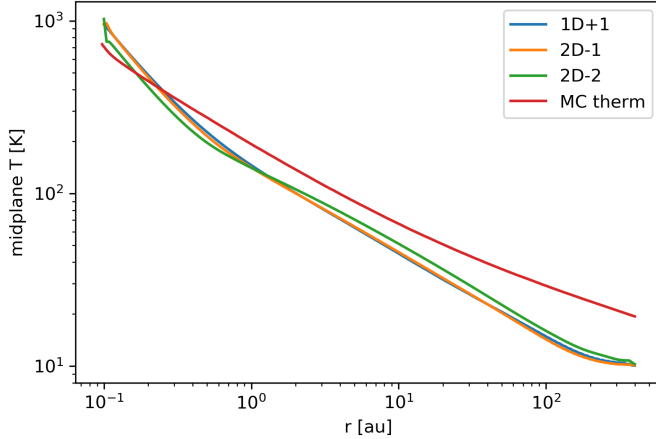


Figure 5.4: The mid plane temperatures according to the different methods. The MC therm shows the temperature for the mid-sized dust grain

5.3 Radial Intensity

With a given density and temperature setup, one can calculate the radial intensity of the disk at different wavelengths.

In the mm continuum emission, the radial intensity obtained by the three setup techniques agree very well with each other. Radial intensity found with the temperature set by full radiative transfer (MC therm) has a lower intensity by about a factor of 2 and the difference increases slightly in the outer parts of the disk. One reason for this is that a minimum temperature has not been set for the MC therm calculation. For the other techniques a minimum temperature of 10K has been used considering the ambient temperature in a star forming region. This would make a difference in the outer parts of the disk where heating due to the star is least effective and this is also where the maximum difference is expected and observed.

Fig 5.6 shows the comparison in the radial intensity of the scattered light (H band). The scattered light is not very sensitive on the final temperature but more on the vertical structure. The 2D-2 approach and the MC therm approach both have the same preliminary vertical structure setup with MC therm just having a final different temperature calculation and as a result both have an identical radial intensity profile. The 1D+1 and the 2D-1 approach though have a slightly lower intensities suggesting that the scattering surface of the disk is flatter compared to the one in the 2D-2 approach. This seems to be consistent with the vertical profiles shown earlier (Fig 5.1).

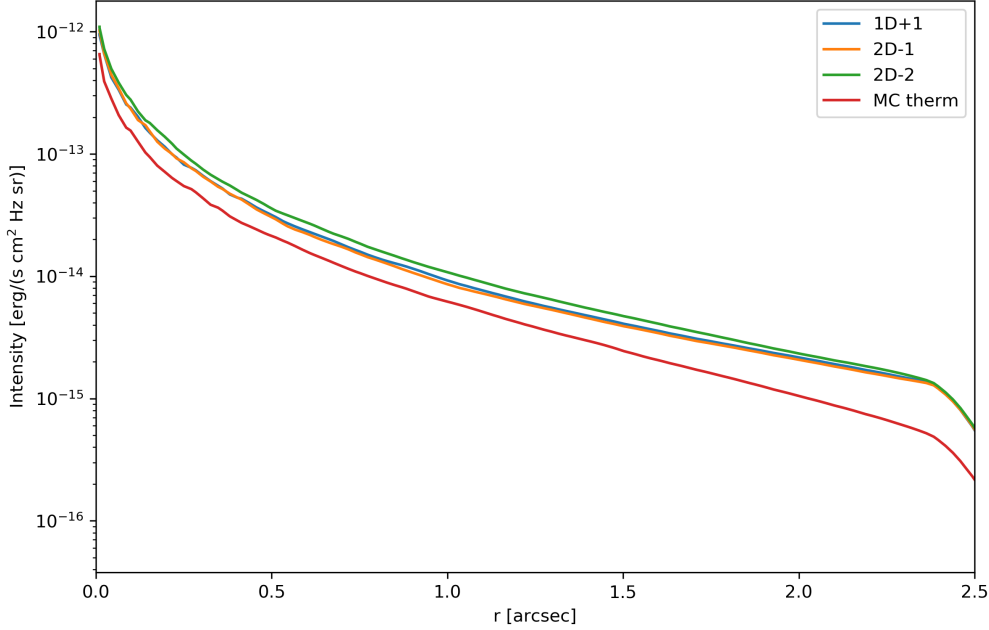


Figure 5.5: The radial intensity profile in the 1.25mm. Intensities obtained by using the different diffusion temperature calculations are consistent with each other but seem to be higher compared to the one calculated through a full radiative transfer temperature calculation

5.4 Setup Time

Since it has been established that the three setups don't deviate from each too much in terms of the density, temperature and the radial intensity profiles, it is interesting to note how long it takes for each of the individual setup (table 5.1). 1D+1 and 2D-1 take about the same time ~ 20 s but 2D-2 takes 13.5 times (273s) longer. In addition if one wants to use the full radiative transfer for the temperature calculation it requires 3min 10s. Therefore if the full radiative transfer temperature calculation is used iteratively (5 iterations are needed at the very least), the disk would need about 16min to be setup which would be extremely long if one were to use an iterative method to calculate the most optimum parameters of the disk.

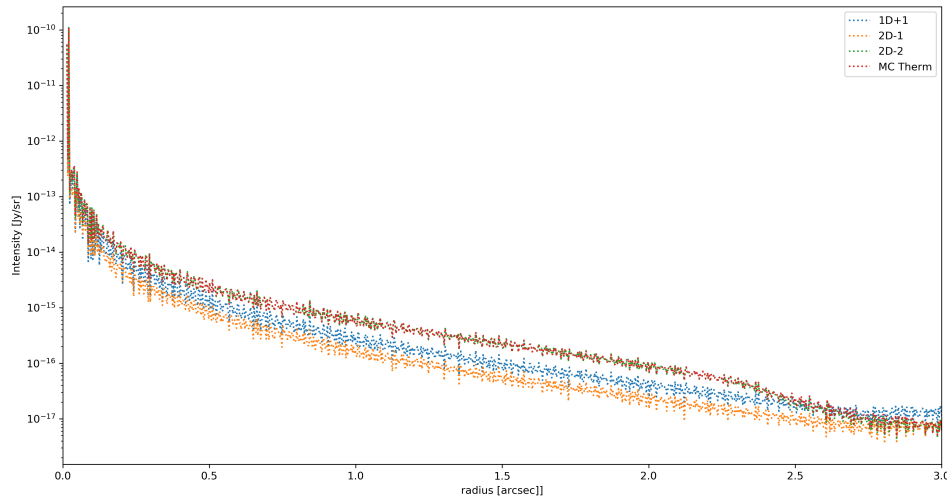


Figure 5.6: The radial intensity profile in the scattered light

1+1D	19.6s
2D-1	21.8s
2D-2	4min 33s
Full radiative transfer	3min 10s

Table 5.1: Time taken by the three setups and the full radiative transfer temperature calculation

Chapter 6

Images and Radial Intensity Profiles

In chapter 5, the radial intensity profiles in the mm continuum and scattering light obtained by the different setups were shown. This chapter deals with how these were calculated and also what the intensity profiles of the actual observations are. The actual process of making images from a given physical disk setup is done by RADMC-3D and has been discussed in chapter 3.

6.1 Synthetic Images

The images from the models are shown in fig 6.1. As expected the mm continuum image like the one from DSHARP (fig 1.1) shows a flat disk whereas the scattered light image shows a flared profile and an asymmetry with the near side of the disk appearing brighter than the further side, again similar to the DARTTS-S observation (fig 1.2).

6.2 Radial Profiles

This work uses a comparison of the radial intensity profiles as the way to find the most optimum model. Finding the radial intensity profile for a flat disk is straightforward. The intensity along the semi major axis, given the position angle of the disk has been taken. To find the intensity profile of a flared disk, one needs to first deproject it. For the deprojection an estimate of the scattering surface is required. The scattering surface is parametrised with the flaring index α .

$$\frac{h}{r} = \frac{h_o}{r_o} \left(\frac{r}{r_o} \right)^{(\alpha-1)} \quad (6.1)$$

This is similar to eq 4.4. [3] mentions the value of α for IM Lup as 1.27 ± 0.20 and the value of h/r being 0.18 ± 0.03 at a radius of 100au. These values have been used and the tool used is imagecube (<https://github.com/richteague/imgcube>) developed by Richard Teague.

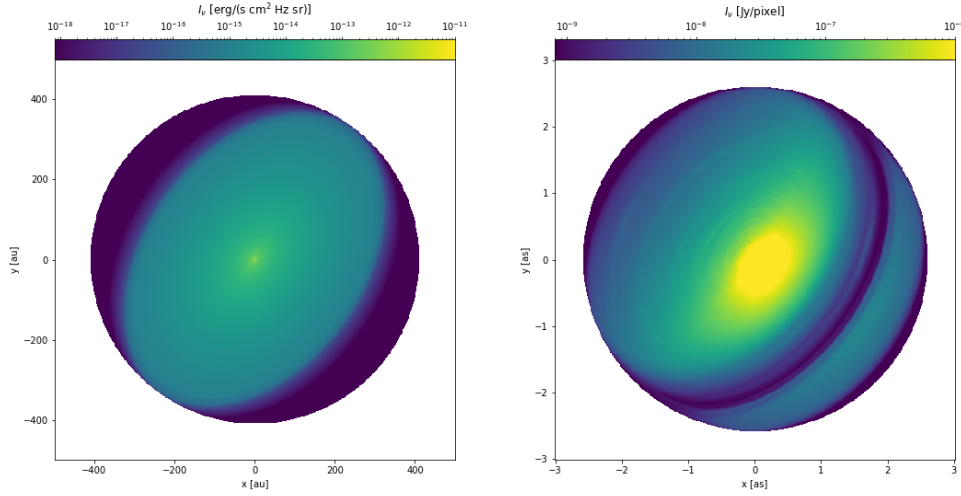


Figure 6.1: The mm continuum image (left) and the scattered light image (right) based on the parameters mentioned in chapter 5

The radial profiles for both the wavelengths are shown in fig 6.2 and fig 6.3. In these plots the radial intensity profiles obtained from the synthetic images of the model (fig 6.1) are also plotted.

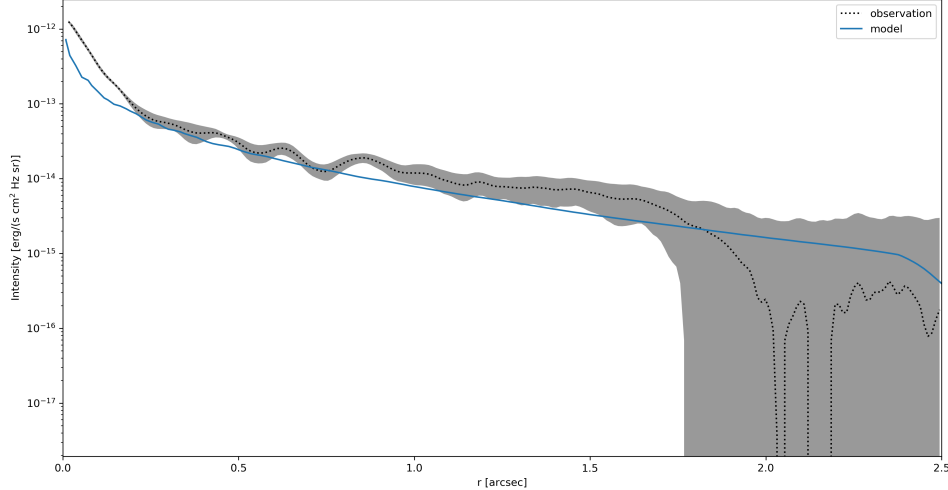


Figure 6.2: The radial intensity profile mm continuum

The following subsections test out how some of the disk parameters impact the radial

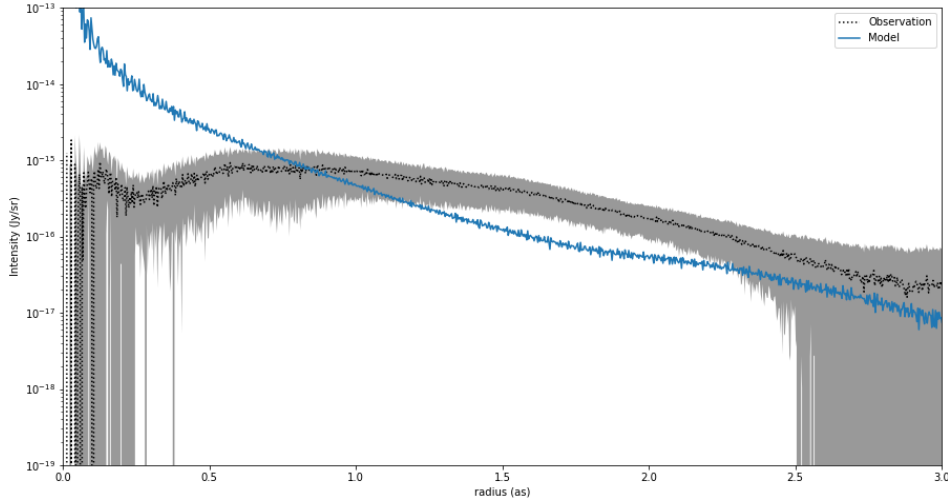


Figure 6.3: The radial intensity profile in the scattered light

intensity profiles.

6.2.1 Disk Mass

To understand the effect of disk mass (and as a consequence dust mass, since dust mass is 1% of the disk mass). The previously modeled disk with a disk mass of 11% of the star mass has been compared to a disk with half the mass. The radial intensity profiles are in fig 6.4 and 6.5.

The mm continuum has an almost parallel shift in the outer parts of the disk, with the low mass having an intensity of about 1.5 times less than that of the high mass disk. This is expected since there are fewer dust grains emitting and given that the disk is expected to be optically thin in the outside the first few AU from the star. This is the reason why the mm flux is often used as a proxy to estimate total dust mass in a disk.

The scattered light intensity doesn't show much difference between the two disks.

6.2.2 Grain Sizes

A similar test with two disks of varying q parameter (eq 3.1) was carried out. A high value of q would imply more mass in the larger sized dust grains. A value of $q = 4$ would mean same amount of mass in all dust grains. A disk with $q = 3.5$, a value which is typically considered, is compared with a disk with $q = 3.9$ i.e. dust with similar mass distribution across the different sizes. Note that eq 3.1 shows the relation of number by particle size with exponent q . if one were to express the relation between surface density by particle

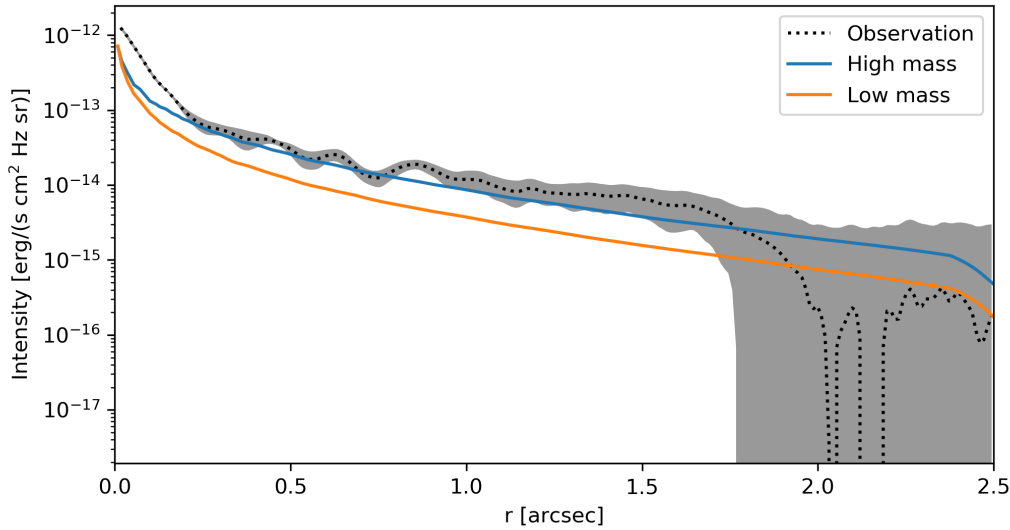


Figure 6.4: The radial intensity profile comparison for disk of different masses in the mm continuum

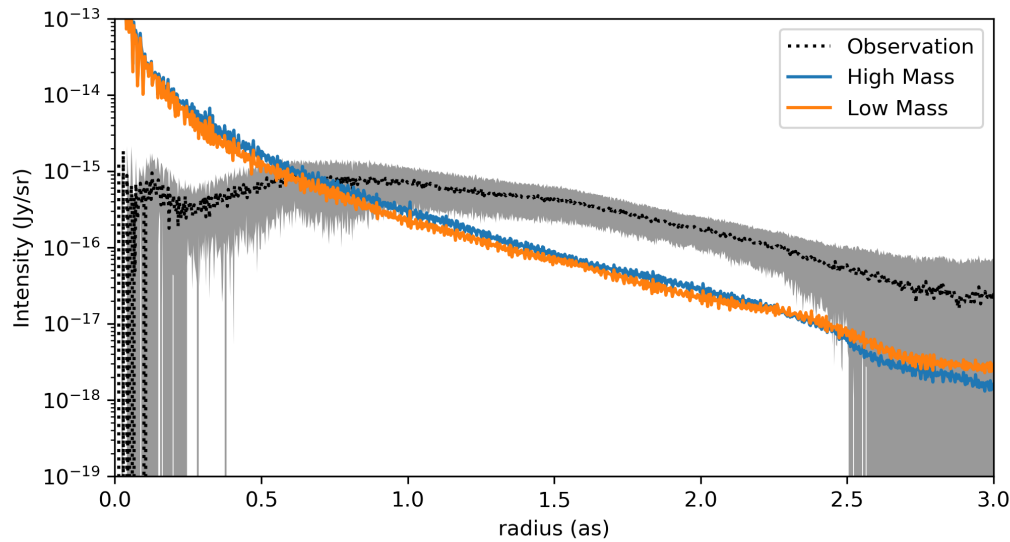


Figure 6.5: The radial intensity profile comparison for disk of different masses in the scattered light

size the exponent would be $4 - q$.

Fig 6.6 and 6.7 show the radial intensity profiles for these two disks. The mm continuum has a higher intensity for a higher value of q suggesting that the emmission is higher

for dust with larger size. The relationship is reversed in the scattering light image. Scattering intensity is dominated by smaller dust grains further away from the disk-midplane. Therefore it is not surprising that increasing the proportion of smaller grains increases the intensity in the scattered light.

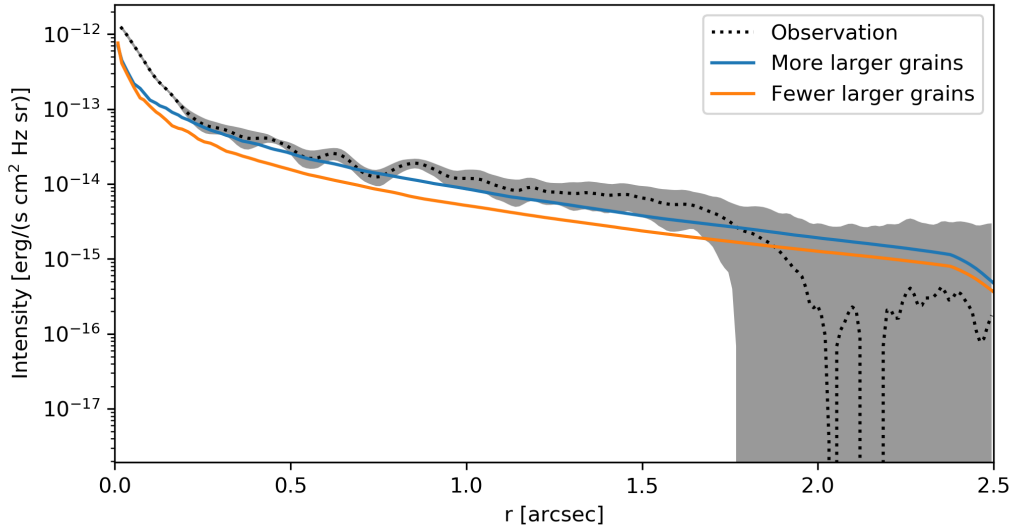


Figure 6.6: The radial intensity profile comparison in the mm continuum for disk with different amount dust in different grain sizes

These two tests suggest that finding the optimum parameters might not be straightforward. The proportion of large grains in the two wavelengths shows a reverse behaviour and trying to get a better fit for one might reduce the goodness of fit for the other. The mass test, despite seeming to have a more straightforward relationship, also cannot be used without limitations. The disk mass is typically 10% of the star mass above which the disk starts to become gravitationally unstable. The base case for the above tests already uses 11% disk mass and increasing this mass much further might not be physically possible. Therefore instead of looking for the optimum parameters through hand and intuition, a computational method is used.

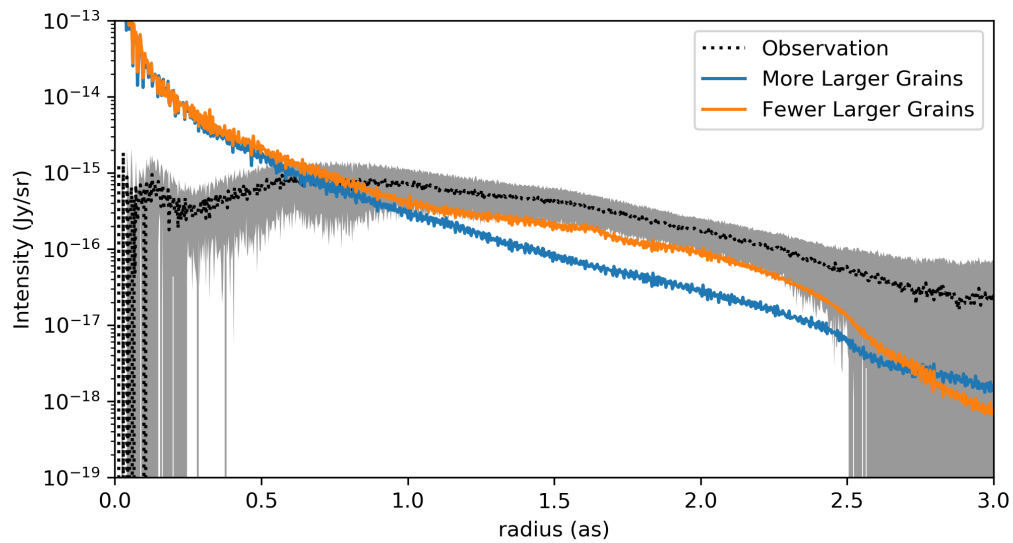


Figure 6.7: The radial intensity profile comparison in the scattered light for disk with different amount dust in different grain sizes

Chapter 7

Monte Carlo Markov Chains and Parameter Estimation

The Monte-Carlo Markov Chain (MCMC) is an algorithm which is used to sample the parameter space of a given model. The dust distribution model in our protoplanetary disk can essentially be characterised by a set of parameters. These relate to the radial density (eq 4.1), distribution across sizes (eq 3.1), maximum particle size (eq 4.20) and the dust to gas ratio. In the previous chapter, it was seen that the impact of the these different parameters is not always straightforward and they might be working together or against each other when it comes to obtaining a good fit of the radial intensity in the two wavelengths. An algorithm like the MCMC could be used to find out the most likely values of the parameters given the observation and the uncertainty around the most likely value.

7.1 The χ^2 value

Given a certain set of parameters Θ , the likelihood that a given set of parameters fit the observed data D comes from the Bayes' Theorem

$$p(\Theta|D) = \frac{p(\Theta)p(D|\Theta)}{\int p(\Theta)p(D|\Theta)d\Theta} \quad (7.1)$$

If we have an observation y , we assume that y follows a Gaussian distribution around the average of all observed values.

$$p(y) = \frac{\exp(-(y - \bar{y})^2/2\sigma^2)}{\sqrt{2\pi}\sigma} \quad (7.2)$$

In our particular case y is what we get from the observation and σ is the error/uncertainty associated with this. \bar{y} is the measurement value we get from our model for a given set of input parameters Θ . Which means that $p(y)$ is the probability of how good the data fits given our model. In fact the correct notation would be $p(y|\Theta)$. If the σ is large then

a higher difference between y and \bar{y} is acceptable in order to have the same probability. If we have multiple measurement points for a given model we can represent the whole thing as a product

$$p(y_1, y_2, \dots, y_N | \Theta) = \prod_{i=0}^N \frac{\exp(-(y_i - \bar{y}_i)^2 / 2\sigma_i^2)}{\sqrt{2\pi}\sigma_i} \quad (7.3)$$

The $p(y_1, y_2, \dots, y_N | \Theta)$ is analogous to the $p(D | \Theta)$ in eq 7.1. Therefore we have the probability of the data given the parameters. We use eq 7.1 to switch this around and find out the probability of the parameters given the data $p(\Theta | D)$. The two quantities are proportional to each other. The integral in the denominator is a constant and $p(\Theta)$ is also taken as a constant since without observed data, all parameter values are just as likely.

$$p(\Theta | D) \propto \exp(-\chi^2(D)/2) \quad (7.4)$$

where

$$\chi^2(D) = \sum_{n=1}^N (y_i - \bar{y}_i)^2 / \sigma_i^2 \quad (7.5)$$

Therefore the negative log of the probability is proportional to the χ^2 value

$$\chi^2(D) = -\log(p(\Theta | D)) \quad (7.6)$$

Therefore χ^2 is a metric which indicates how good a fit is given a set of parameters and the task is to find such a set of parameters which minimize the χ^2 and as a result maximise the probability of the parameters giving a good fit. Additionally a distribution of the possible parameters can also be obtained based on how the χ^2 changes with the change in parameters.

7.2 MCMC Algorithm

The algorithm used to sample the parameter space and make a Markov chain is the **stretch-move** algorithm [11] carried out by the Python library **emcee** [9]. The algorithm is described below

1. Start with K walkers. In this work K is taken as 20. The set of all parameters of the K walkers is S_k . The set of all parameters without a particular walker k is termed $S_{[k]}$
2. Each walker has a position i.e. a set of values for all the input parameters (The number of parameters is also referred to as the number of dimensions N). The walker k with position X_k is picked. A new position Y is then proposed in the following way

$$Y = X_j + Z[X_k - X_j] \quad (7.7)$$

X_j is the position of a random walker from the remaining walkers $S_{[k]}$. Z is a number randomly drawn from a distribution $g(z)$ which is typically taken as

$$g(z) = \begin{cases} \frac{1}{\sqrt{z}}, & \text{if } z \in [a, \frac{1}{a}] \\ 0, & \text{otherwise} \end{cases} \quad (7.8)$$

a is an adjustable scale parameter whose value indicates how large the steps between the original and the proposed move should be. It is taken by default as 2.

3. The proposed new position Z is accepted based on the probability

$$q = \min \left(1, Z^{N-1} \frac{p(Y)}{p(X_k)} \right) \quad (7.9)$$

If the move is accepted then Y becomes the new value of X_k otherwise it stays the same

4. Steps 1-3 are then repeated for all the walkers n number of times (number of steps) in order to obtain the required number of samples.

If the walkers start from a position which is highly improbable then an appropriate number of *burn-in* steps might be required in order to make sure they reach a more probable part of the parameter space. For our model, it was seen that a burn-in of about 100 steps seems to be sufficient for the chains to start converging around the most probable value.

For the starting position of the parameters, a uniform random number between 0 and 1 has been taken except for Σ_c which could have a uniform probability in the log scale from 10^{-2} to 10^2 . The coefficient of the dust-to-gas ratio when expressed as a power law has a starting value with a uniform random number between 0.5% and 1.5%, since this is typical ratio found in the ISM. The exponent of this power law starts somewhere between -0.5 and +0.5.

Additionally there are some physical constraints that have been put. The surface density cannot be negative. Similarly the amount of dust cannot be negative. The upper limit for the amount of dust is 50%. The upper limit to the mass of the disk has been put as 20% the mass of the star. These values are not explicitly forbidden but the value of the log probability when the walkers have one of these values has been set very low. Which makes these positions practically forbidden and extremely unlikely to be accepted.

7.3 Without scattered light

For the first run, only the radial intensity profile in the mm continuum has been optimised. The following five parameters have been taken

1. Sigma coefficient Σ_c from eq 4.1
2. Sigma exponent γ from eq 4.1
3. Size exponent $(4 - q)$ from eq 3.1. $(4 - q)$ is to represent distribution in terms of surface density instead of number of grains
4. a_{max} coefficient from eq 4.20
5. a_{max} exponent from eq 4.20

100 dust species were considered spaced logarithmically between 10^{-5} and 10^{-1} cm.

The sampler was run for 250 steps. Fig 7.1 shows the log probability as a function of the number of iterations and convergence seems to be achieved by the 100th iteration. There are also a few walkers which are stuck in a part of the parameter space which doesn't make physical sense and as a result give a very low log prob value. These walkers have been removed in the subsequent analysis.

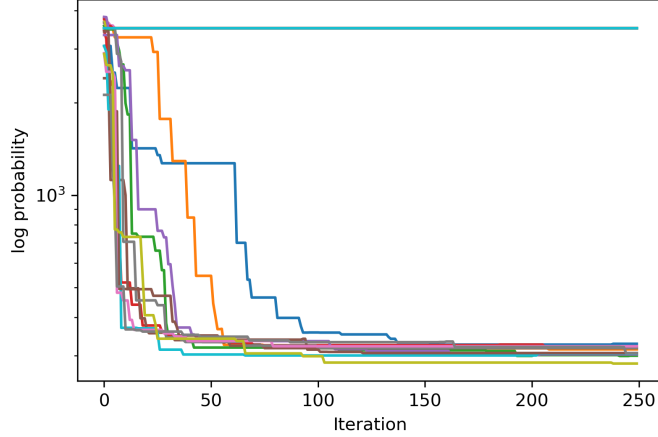


Figure 7.1: The negative of the log probability values for the different walkers by the iteration number. The walkers seem to converge after about 100 steps apart from a few *rouge* walkers

The distribution of the samples can be represented as a corner plot (fig 7.2). The parameters are strongly peaked suggesting the values are well constrained. The values of the expectation value and the uncertainty are given in table 7.1 and the radial intensity plot obtained from using these values is in fig 7.3.

The radial intensity profile of the model matches very well with the observation. The mass of this disk is $0.072M_\odot$ or 10% of the mass of the star. The value of the size exponent (1.26) is much higher than the typical value of 0.5 suggesting a lot more mass in the larger

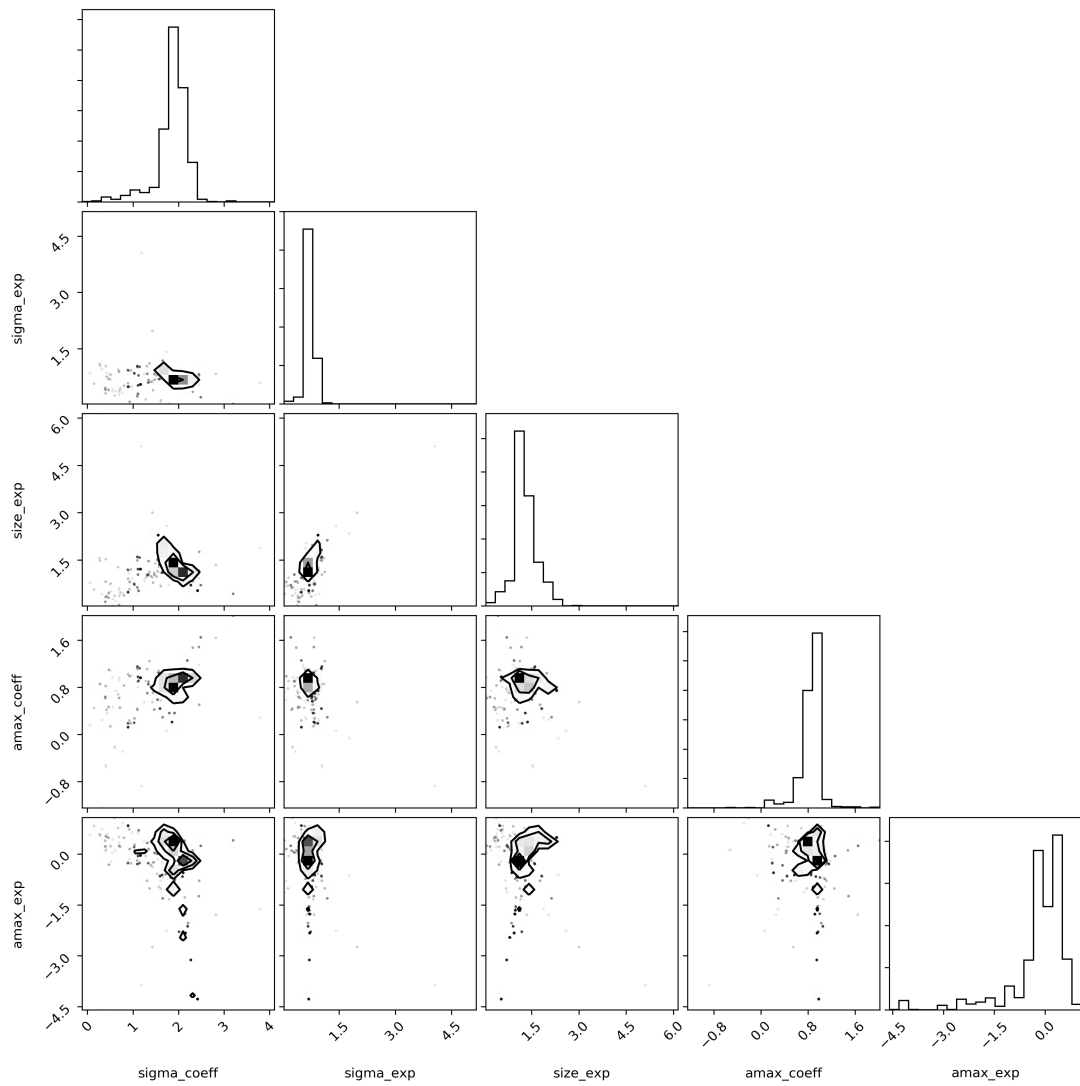


Figure 7.2: The corner plot which shows the distribution of the samples of parameters and their correlations with each other.

Sigma coeff	1.858 ± 0.356
Sigma exp	0.737 ± 0.159
Size exp	1.261 ± 0.365
Amax coeff	0.854 ± 0.196
Amax exp	-0.173 ± 0.853

Table 7.1: Parameter expectation values and standard deviation using a 5 parameter model for the continuum intensity profile

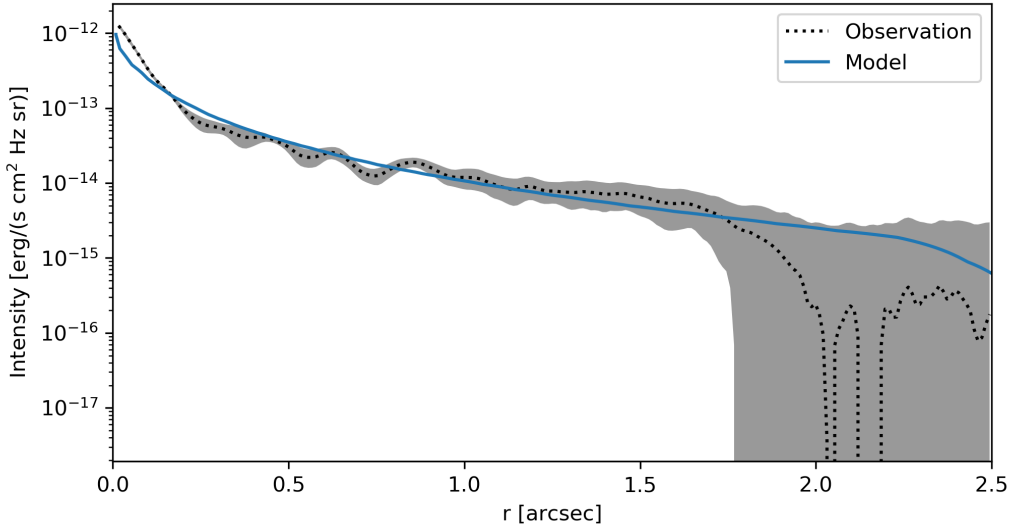


Figure 7.3: The radial intensity profile comparison in the mm continuum for disk with different amount dust in different grain sizes

dust grains. Also the values of A_{max} coeff is such that it is always more than the biggest grain in the model, implying that a_{max} remains the same across the disk radius i.e. 1mm. This value of A_{max} coeff also explains why A_{max} exp is not so strongly constrained since there is a whole range of values where it would have no impact on the a_{max} . Fig 7.4 shows the surface densities of the gas and dust.

The image and the intensity profile in the scattered light for this best fit disk was also plotted (fig 7.5 and fig 7.6). Here, the model is nowhere close to the observation. The disk appears to be flat and not having a strong flaring geometry. This is the result of the model having a high value of the size exponent which greatly reduces the number of smaller dust grains which ideally settle at much higher vertical heights but are mostly absent in this disk. As a result the radial intensity profile is also much weaker than the actual observation.

Considering that the algorithm only optimised on the mm continuum profile and the relation between the parameters and the two intensity profiles is not straight forward, it is not surprising that the fit in the scattered light is quite poor and with a much lower intensity. Therefore it is not enough to just optimise the continuum profile but also the scattering light profile. This has been discussed in the following section.

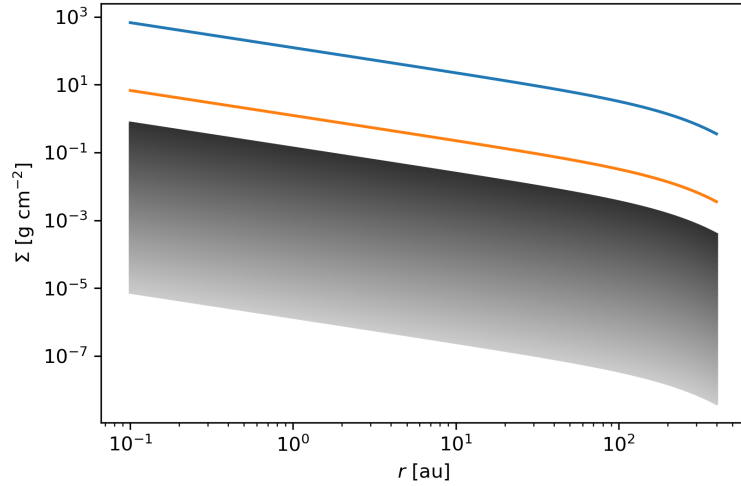


Figure 7.4: The radial density of the gas and dust in the disk with the best fit parameters with the darker shade representing a larger particle size. The a_{\max} stays constant as a function of a radius and the mass in large grains is much larger than that in smaller grains

7.4 With scattered light

One of the reasons for not including the scattered light observation as a part of the previous optimisation was the amount of time it takes to construct an image with full scattering. If one takes 100 dust species (as was done in the previous section), the time taken to make an image in the scattered light is more than 2 hours (with time scaling linearly with the number of dust species). This would increase the run time of the MCMC by about 50 times. But at the same time it is seen that the scattered light can also not be ignored altogether. As a result, the number of dust species has been reduced from 100 to 5 (still in the same range and spaced logarithmically). In addition, the comparison between the observation and the model is now done only outside the 1arcsec range. This has been done primarily because we are more interested in characterising the dust in the outer parts of the disk where the difference in the geometry between the mm continuum and the scattered light observation is the maximum. The amount of dust present in the outer parts of the disk is an indicator for the disk life times. Additionally, for the scattered light close to the star, it is difficult to distinguish between the disk and the star as the true source of the light. In observation a coronograph is used to block out the starlight, which is why the observed intensity close to star is always much lower than the modelled intensity.

Additionally, two more parameters relating to the dust-to-gas (d2g) ratio were introduced to this MCMC run. Similar to eq 4.20 the d2g ratio has also been written out as a power law with a coefficient and an exponent. The parameters are initialised in such a way that the d2g coeff has a uniform random value between 0.5% and 1.5% and the d2g

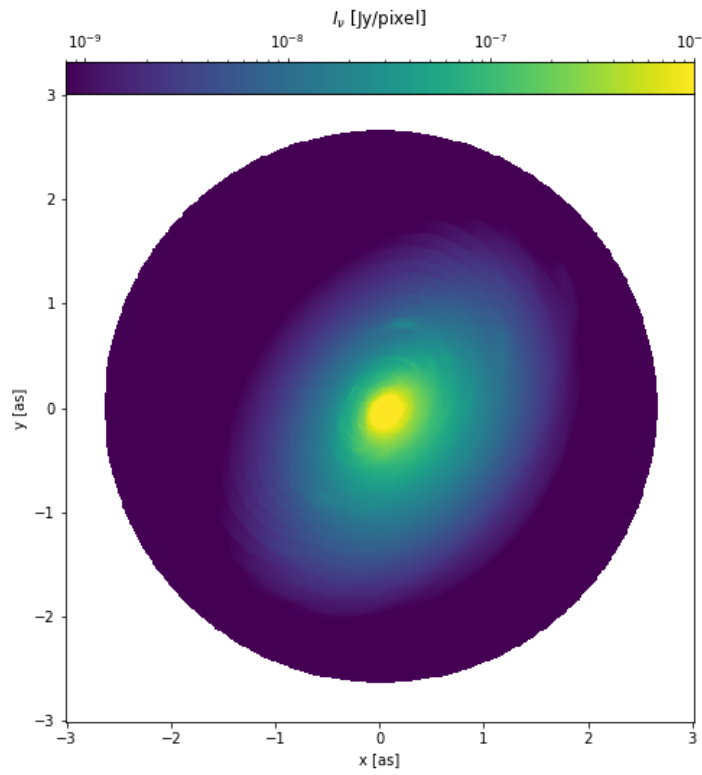


Figure 7.5: The image of the modelled disk in the scattered light. The flared geometry is not present and the radial extent of the disk is quite reduced

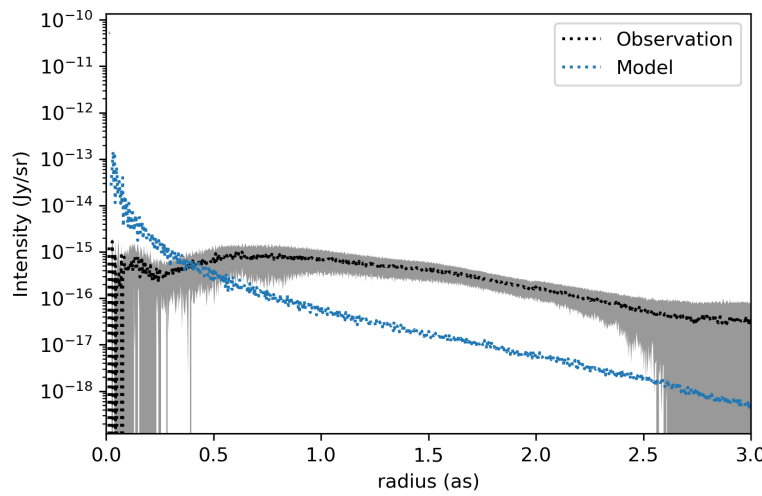


Figure 7.6: The radial intensity in the scattered light is much lower than the observation

\exp has a uniform random value between -0.5 and 0.5.

The corner plot for this simulation run is shown here.

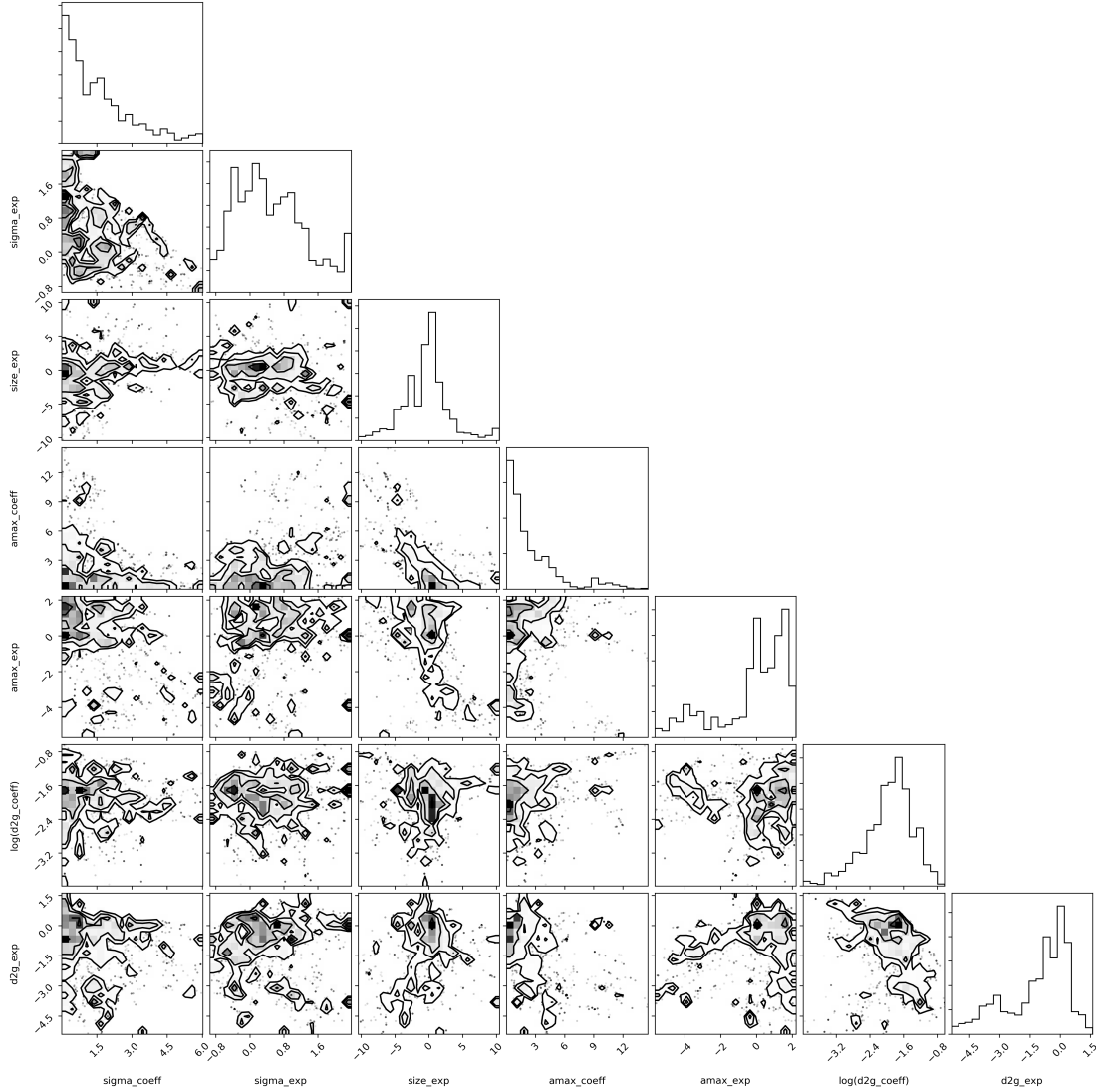


Figure 7.7: The plots show that the parameters are not as tightly constrained as the case where the scattering light was not included

The values of the parameters in table 7.2 and the corner plot show that the estimated parameters are not very well constrained. The expected value of Sigma coeff and Sigma exp are not very different from those obtained from section 7.3. But for the other parameters the values are very different and the uncertainty associated with all the parameters is also very large. The Size exp has a negative expected value which suggests that smaller dust grains contain more mass than larger dust grains. Also, note the extremely high uncer-

Sigma coeff	1.598 ± 1.442	Sigma exp	0.494 ± 0.820
Size exp	-0.362 ± 3.593		
Amax coeff	2.546 ± 2.803	Amax exp	-0.215 ± 1.987
d2g coeff	0.023 ± 0.030	d2g exp	-1.122 ± 1.577

Table 7.2: Parameter expectation values and standard deviation using a 7 parameter model. The parameters are a lot less constrained than the previous run

tainty in this value. The negative value of the d2g exp suggests that the dust to gas ratio decreases in the outer part of the disk which is something expected given the radial drift inwards of the dust grains.

The profiles obtained from using the expected value of the parameters actually show a huge mismatch in the model and the observation especially in the continuum profile. This is a consequence of the low disk mass (7% of star mass), low dust to gas ratios in the outer parts of the disk and low proportions of large grains.

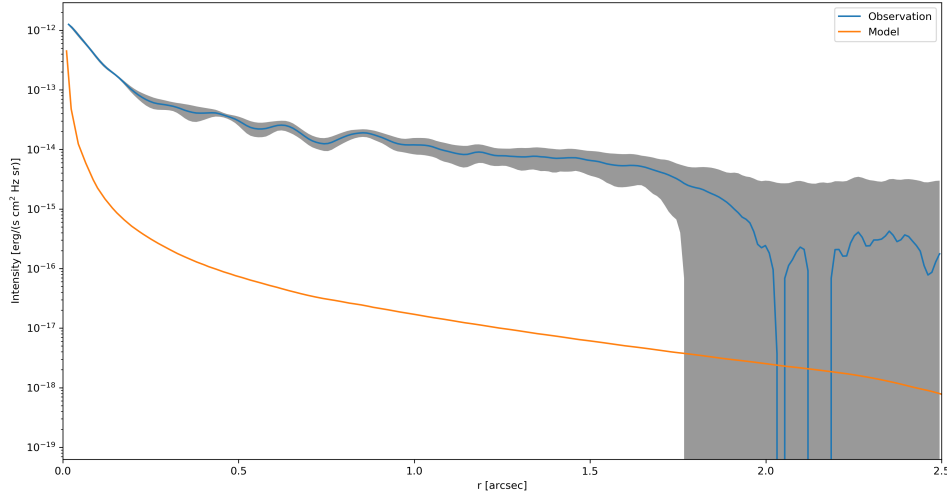


Figure 7.8: The mm continuum profile of the modelled disk with the mean parameters is much lower than the observation

The log probability value (scaled to a random value) is -2.84. The log probability values for the different walkers of the MCMC suggest that this is the typical value of the obtained by the MCMC (fig 7.10). The limit around 3 is obtained when the modelled intensity is negligible compared to the observation, so it is a limit on the log prob function when the intensity is very low. It is surprising to see that there are walkers which manage to reach areas with a much higher probability but after a few steps return to regions with lower

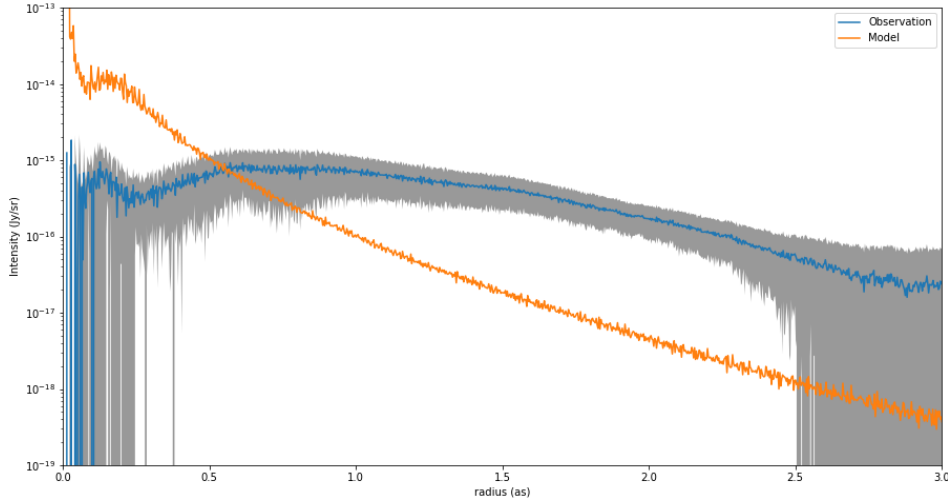


Figure 7.9: The scattered light intensity profile for the disk with the mean parameters is also deficient

probability.

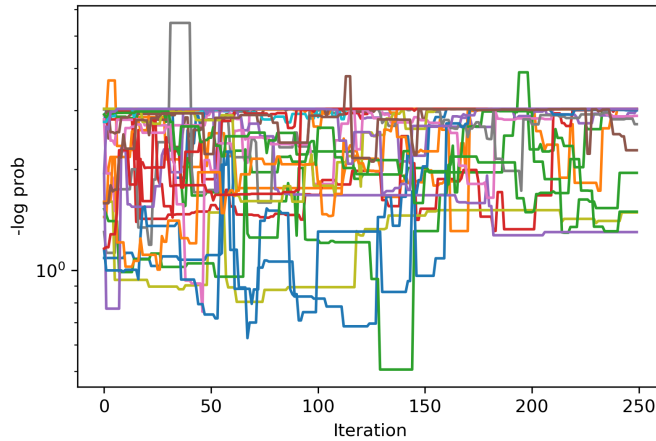


Figure 7.10: The plots show that the parameters are not as tightly constrained as the case where the scattering light was not included

Through fig 7.11, we can see that the samples are not constrained at all. Here 500 random samples are taken from our MCMC output. The radial profiles of the total dust density and the dust to gas ratio are plotted. The total dust density spans a range of three orders of magnitude in the outer parts of the disks. The dust to gas ratio is constrained

even worse with a span of 10 orders of magnitude.

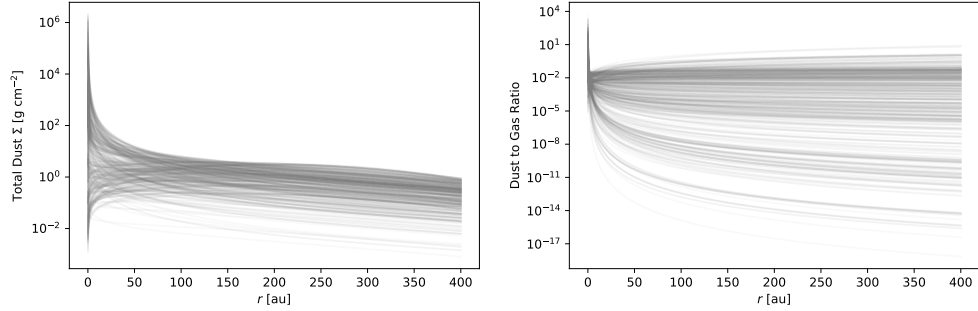


Figure 7.11: The profiles of the total dust density and the dust to gas ratio for 500 random disks obtained from the MCMC output parameter samples

The highest log prob obtained during the MCMC was -0.51 and the obtained profiles are shown below. The fits are much better. But this gives only one set of possible values of the parameters and not the uncertainty around these values.

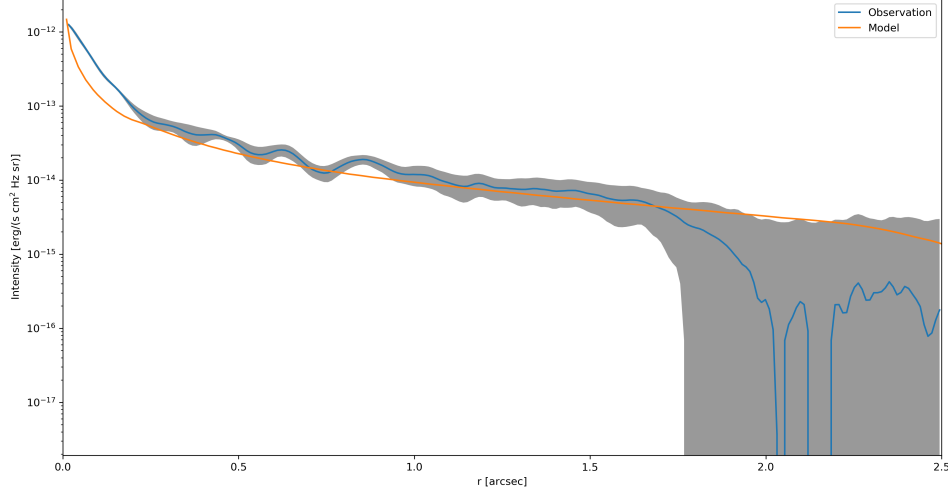


Figure 7.12: The mm continuum profile of the modelled disk with the highest probability

Since the algorithm optimised only on the intensity profiles, some of the physical features of the disk are not intuitive despite the intensity profiles being a very good match. This disk has a high mass i.e. 16.6% of the star mass. At such a mass the disk would start becoming gravitationally unstable. The value of the size exp is highly negative which

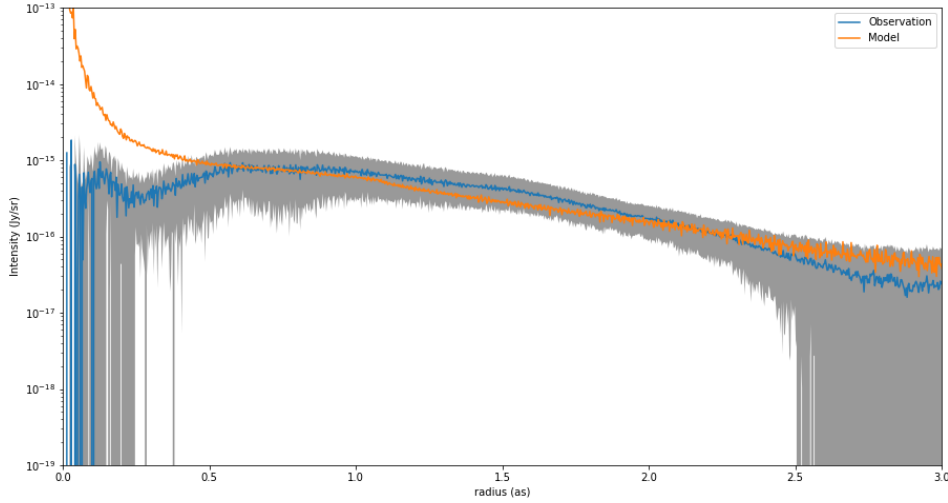


Figure 7.13: The scattered light intensity profile for the modelled disk with the highest probability

Sigma coeff	3.099	Sigma exp	0.702
Size exp	-2.417		
Amax coeff	1.089	Amax exp	1.896
d2g coeff	0.013	d2g exp	0.130

Table 7.3: Parameter values of the model with the highest probability

means an abnormally large proportion of mass in the smaller dust grains. The dust to gas exp is also positive which makes the dust to gas ratio increase moving away from the star which is inconsistent with radial drift.

Since most of the samples from the MCMC are not good fits to the observed intensity, a statistical analysis of the samples and the disks obtained from them has not been done. The possible reasons for the MCMC failing to provide samples with better fits has been discussed in the next chapter.

Chapter 8

Conclusion

In the previous, we saw that the parameters of the disk properties could not be successfully constrained. Most of the samples obtained through the MCMC do not fit well to the observed intensity profiles. The possible reasons for this could be one or both of the following

1. *The shape of the probability curve as a function of the parameter values* - It could be that the probability curve is very flat in most parts of the parameter space with just a few sharp but not very strong peaks. It would be hard for the crawlers to find these peaks if they are sharp and once they are found it would be hard for the crawlers to stay there if they are not very strong. In such a case the possible solution could be to change the MCMC algorithm in which a different kind of move instead of the currently used stretch move
2. *Disk Setup* - There are various assumptions made while setting up the disk model and before putting it through MCMC. For example, limiting the number of dust species to 5 might be too few. The relationship between the parameters and the physical quantity has been always taken as a power law which might not be the case. The number of parameters going into the the model might also not be sufficient. Parameters like the viscosity coefficient and the minimum particle size might also need to be optimised

The next steps for this work would be to address these potential problems and if an appropriate set of parameters is obtained, to look at some statistical properties of the samples like the disk vs dust mass, large dust vs small dust mass and so on.

The codes used in this work are available at <https://github.com/aniruud/IMLup>.

References

- [1] J.M. Alcalá, C.F. Manara, A. Natta, A. Frasca, L. Testi, B. Nisini, B. Stelzer, J.P. Williams, S. Antoniucci, K. Biazzo, E. Covino, M. Esposito, F. Getman und E. Rigliaco, *Astron. & Astrophys.* **600** (2017), A20.
- [2] S.M. Andrews, J. Huang, L.M. Pérez, A. Isella, C.P. Dullemond, N.T. Kurtovic, V.V. Guzmán, J.M. Carpenter, D.J. Wilner, S. Zhang, Z. Zhu, T. Birnstiel, X.N. Bai, M. Benisty, A.M. Hughes, K.I. Öberg und L. Ricci, *Astrophys. J. Letters* **869** (2018), L41.
- [3] H. Avenhaus, S.P. Quanz, A. Garufi, S. Perez, S. Casassus, C. Pinte, G.H.M. Bertrang, C. Caceres, M. Benisty und C. Dominik, *Astrophys. J.* **863** (2018), 44.
- [4] T. Birnstiel, C.P. Dullemond, Z. Zhu, S.M. Andrews, X.N. Bai, D.J. Wilner, J.M. Carpenter, J. Huang, A. Isella, M. Benisty, L.M. Pérez und S. Zhang, *Astrophys. J. Letters* **869** (2018), L45.
- [5] E.I. Chiang und P. Goldreich, *Astrophys. J.* **490** (1997), 368.
- [6] P. D'Alessio, N. Calvet und L. Hartmann, *Astrophys. J.* **553** (2001), 321.
- [7] B.T. Draine, *Ann. Rev. Astron. Astrophys.* **41** (2003), 241.
- [8] C.P. Dullemond, A. Juhasz, A. Pohl, F. Sereshti, R. Shetty, T. Peters, B. Commercon und M. Flock. *RADMC-3D: A multi-purpose radiative transfer tool*, Feb 2012.
- [9] D. Foreman-Mackey, D.W. Hogg, D. Lang und J. Goodman, *Publications of the Astronomical Society of the Pacific* **125** (2013), 306.
- [10] S. Fromang und R.P. Nelson, *Astron. & Astrophys.* **496** (2009), 597.
- [11] J. Goodman und J. Weare, *Communications in Applied Mathematics and Computational Science* **5** (2010), 65.
- [12] T. Henning und R. Stognienko, *Astron. & Astrophys.* **311** (1996), 291.
- [13] C.D. Levermore und G.C. Pomraning, *Astrophys. J.* **248** (1981), 321.
- [14] J.S. Mathis, W. Rumpl und K.H. Nordsieck, *Astrophys. J.* **217** (1977), 425.

- [15] S.Z. Takahashi und S.i. Inutsuka, *The Astronomical Journal* **152** (2016), 184.
- [16] F. van Leeuwen, *Astron. & Astrophys.* **474** (2007), 653.
- [17] S.G. Warren und R.E. Brandt, *Journal of Geophysical Research (Atmospheres)* **113** (2008), D14220.

Acknowledgments

Science never takes place in isolation. This work is no exception. Despite having only one name on the front page, it would not have been possible without the invaluable contribution of many people.

The biggest thanks goes to my supervisor, Til, who has invested so much time and effort for me. He has been extremely patient and understanding. Discussions with him have been extremely useful. I have learnt a lot from him both in theory and in practice.

In this work, I used plenty of code which has not been developed by me but I am extremely grateful for. Thanks to Kees Dullemond for RADM-3D and DISKLAB, Richard Teague for Imagecube and Til (again) for the DSHARP opacities and DISKLAB.

The members of the research group have been both a source of encouragement and entertainment. Thanks for the lunch company, interesting discussions and all the cake.

Gratitude also goes to the staff at the USM for the smooth running of the hardware and software I have used for this work.

And of course, I thank my parents, who have always been supportive of everything that I have wanted to do even if it meant moving very far away and doing something unconventional.

Declaration:

I hereby declare that this thesis is my own work and that I have not used any sources and aids other than those stated in the thesis.

München, 11.03.2020

Anirudh Sharma

List of figures

1.1	The 1.25mm continuum image from DSHARP survey (left) and the radial intensity profile in mJy beam ⁻¹ (right). D117 and B134 are the dark and bright bands respectively identified by DSHARP	2
1.2	H-band image for IM Lup as obtained from DARTTS-S	3
3.1	Effective optical constants of the dust [4] with n being the absorption contribution and k being the scattering contribution to the opacity. Together they contribute to the refractive index	12
4.1	The radial density of the gas and dust in the disk which extends till 400au. The critical radius is 300au, Σ_c is 2.6gm/cm ² and γ is 0.87. The grey lines are the surface densities of 10 dust species in the disk with the darker lines corresponding to larger dust sizes.	16
4.2	The radial density of a disk with parameters similar to fig 4.1 but containing a hundred dust species logarithmically spaced between 10^{-5} and 10^{-1} cm with the darker shade representing a larger particle size. As one moves away from the star the darker shades start to disappear and the smaller sized particles start having a larger proportion of the total dust density. The total dust density remains 1% of the gas density	20
4.3	The plot shows the same information as the previous plot. But this time the colours represent the density, with darker colours representing a higher density. The larger particles, which are higher on the y axis, stop being present in the disk after a certain a radius with the cut-off radius being smaller for larger dust grains	20
5.1	The density profiles of the dust obtained by different vertical settling methods	22
5.2	The temperature profiles within the disk by different vertical settling methods	23
5.3	The vertical density and the temperature at a distance of 51.89au from the star	23
5.4	The mid plane temperatures according to the different methods. The MC therm shows the temperature for the mid-sized dust grain	24

5.5	The radial intensity profile in the 1.25mm. Intensities obtained by using the different diffusion temperature calculations are consistent with each other but seem to be higher compared to the one calculated through a full radiative transfer temperature calculation	25
5.6	The radial intensity profile in the scattered light	26
6.1	The mm continuum image (left) and the scattered light image (right) based on the parameters mentioned in chapter 5	28
6.2	The radial intensity profile mm continuum	28
6.3	The radial intensity profile in the scattered light	29
6.4	The radial intensity profile comparison for disk of different masses in the mm continuum	30
6.5	The radial intensity profile comparison for disk of different masses in the scattered light	30
6.6	The radial intensity profile comparison in the mm continuum for disk with different amount dust in different grain sizes	31
6.7	The radial intensity profile comparison in the scattered light for disk with different amount dust in different grain sizes	32
7.1	The negative of the log probability values for the different walkers by the iteration number. The walkers seem to converge after about 100 steps apart from a few <i>rouge</i> walkers	36
7.2	The corner plot which shows the distribution of the samples of parameters and their correlations with each other.	37
7.3	The radial intensity profile comparison in the mm continuum for disk with different amount dust in different grain sizes	38
7.4	The radial density of the gas and dust in the disk with the best fit parameters with the darker shade representing a larger particle size. The a_{max} stays constant as a function of a radius and the mass in large grains is much larger than that in smaller grains	39
7.5	The image of the modelled disk in the scattered light. The flared geometry is not present and the radial extent of the disk is quite reduced	40
7.6	The radial intensity in the scattered light is much lower than the observation	40
7.7	The plots show that the parameters are not as tightly constrained as the case where the scattering light was not included	41
7.8	The mm continuum profile of the modelled disk with the mean parameters is much lower than the observation	42
7.9	The scattered light intensity profile for the disk with the mean parameters is also deficient	43
7.10	The plots show that the parameters are not as tightly constrained as the case where the scattering light was not included	43
7.11	The profiles of the total dust density and the dust to gas ratio for 500 random disks obtained from the MCMC output parameter samples	44

7.12 The mm continuum profile of the modelled disk with the highest probability	44
7.13 The scattered light intensity profile for the modelled disk with the highest probability	45

List of Tables

1.1	Basic properties of the IM Lup. All values apart from the position are from [1]	1
5.1	Time taken by the three setups and the full radiative transfer temperature calculation	26
7.1	Parameter expectation values and standard deviation using a 5 parameter model for the continuum intensity profile	37
7.2	Parameter expectation values and standard deviation using a 7 parameter model. The parameters are a lot less constrained than the previous run . .	42
7.3	Parameter values of the model with the highest probability	45

